Determining the drivers of suspended sediment dynamics in tidal marsh-influenced estuaries using high-resolution ocean color remote sensing

The content of this chapter was published in 2020 in *Remote Sensing of Environment*. This paper was co-authored by Cédric G. Fichot, Carly Baracco, Sergio Fagherazzi (Department of Earth and Environment, Boston University), Neil Ganju (Woods Hole Coastal and Marine Science Center, USGS), Ruizhe Guo, Sydney Neugebauer, Zachary Bengtsson (NASA DEVELOP National Program).

1.1 Introduction

Shallow bays surrounded by salt marshes are a buffer zone between the land and the ocean. These bays protect biodiversity, enhance water quality, mitigate river floods, protect from storms and sequester carbon (Fagherazzi et al. 2012; Fagherazzi et al. 2013b; Kirwan et al. 2016). Salt marshes are nourished with sediment by tides and maintain their elevation with respect to sea level if sediment inputs are adequate (Fagherazzi et al. 2013a; Ganju et al. 2017; Kirwan and Murray. 2007). Sediment deficiency in coastal waters has become widespread in the last century because of sediment trapping in upstream dams and soil conservation practices (Dai et al. 2016; Syvitski et al. 2009; Walling 2006; Yang et al. 2011). Variations in riverine sediment inputs and associated suspended sediment concentration (SSC) could exert a pronounced influence on the morphological stability of the intertidal landscape and its ecosystems. SSC are associated with lower oxygen concentration especially in the estuarine turbidity maxima zone, and affects the spatial distribution of algal blooms by inhibiting algae growth (Carr et al. 2016; Hudson et al.

2017; De Swart et al. 2009). Reduced riverine sediment inputs could starve shorelines leading to wetlands loss (Blum and Roberts 2009; Fagherazzi et al. 2015). SSC data are also instrumental for the reliable calculation of sediment budgets in coastal systems (Ganju et al. 2015). It is therefore imperative to accurately measure SSC in marsh-influenced estuaries (Lawson et al. 2007).

The dynamics of estuarine suspended sediment transport has been extensively studied using in-situ measurements (Dyer et al. 2004, Li and Zhang 1998, Fagherazzi et al. 2017), lab flume experiments (Widdows et al. 1998), and numerical modeling (Fagherazzi et al. 2012; van der Wegen. 2013). Recent studies have characterized the effect of density driven flows (Traykovski et al. 2000), tidal asymmetry (van der Wegen. 2013), wind-induced waves (Mariotti et al. 2010), stratification and flocculation (Winterwerp. 2002) on sediment dynamics. However, these processes are difficult to study due to limited spatial resolution of field observations and sparse bottom data available for numerical modelling (Staneva et al. 2009, Wiberg et al. 2020). Remote sensing data can bridge this data gap. For example, remote sensing can trace the spatio-temporal variations of turbidity maxima and frontal eddies in estuaries (Hudson et al. 2017; Jay et al. 2015; Ribbe et al. 2018; Everett et al. 2012). In addition, spatial distributions of SSC obtained from remote sensing can be set as initial conditions or used for validation, improving accuracy of numerical modeling (Staneva et al. 2009).

High-quality radiometry from the Landsat-8 OLI and Sentinel-2 MSI now offer the possibility to derive high-spatial-resolution maps of SSC with reasonable accuracy in

nearshore regions. Moderate resolution optical remote sensing (spatial resolution > 300 m) has been extensively used to study suspended sediment dynamics in coastal environments around the world (D'Sa et al. 2007; Miller and McKee 2004; Mao et al. 2012; Cao et al. 2017; Hudson et al. 2017; Fettweis and Nechad 2010; Eleveld et al. 2014), but has very limited applicability in nearshore coastal areas, and particularly in enclosed bays and estuaries. However, the improved radiometric and spatial resolution of new sensors like the Landsat-8 OLI (30-m spatial resolution) of Sentinel-2 MSI (10-m spatial resolution) can now facilitate the study of suspended sediments dynamics in such nearshore environments. For instance, Gernez et al. (2015) used such data to explore the influence of river topography and tidal shoals geometry on the distribution of SSC in the Gironde and Loire estuaries. Vanhellemenont and Ruddick (2014) also used remote sensing to showcase the effects of wind turbines on sediment resuspension in the English Channel, and Snyder et al. (2017) employed similar methods to facilitate the selection of sites for oyster aquaculture. Using airborne imaging spectroscopy (2.5-m spatial resolution), Fichot et al. (2016) illustrated the importance of very-high-spatial-resolution images to study the drivers of turbidity and SSC in wetland channels and bays. None of these studies have directly used remote sensing to quantitatively assess the roles of tides, wind, and river discharge in driving SSC dynamics, particularly in marsh-influenced estuaries. Eleveld et al. (2014) derived SSC maps from 84 full-resolution MERIS data (300-m) over the Westerschelde estuary (Netherlands), but only classified them based on flood-ebb tidal stages and seasons.

Here, we leverage the existing record of high-spatial-resolution data from the Landsat-8 OLI and Sentinel-2 MSI to evaluate whether these images can provide a realistic representation of SSC dynamics in tidal marsh-influenced estuaries, despite the long revisit-time of these sensors. Using the Plum Island Estuary (PIE; Massachusetts, USA) as a representative example, we assess whether this remote-sensing record can provide sufficient spatio-temporal information in such dynamic and heterogeneous coastal systems. In situ measurements are used to develop and validate local and sensor-specific empirical algorithms applicable to OLI and MSI imagery of the Plum Island Estuary. The algorithms are implemented on every clear image obtained between May 2013 and August 2018, and the derived SSC maps were used to quantitatively evaluate the role of river discharge, wind speed and direction, flood-ebb tidal stage, and episodic events of river floods and storms in regulating the SSC distribution along the thalweg of the Plum Island Estuary. A simple model to predict the SSC along the estuary from these physical drivers is also developed and presented.

1.2 Study site

Plum Island Estuary is a tidally-dominated and marsh-influenced estuary that represents the largest saline wetland in New England (Fig. 1.1). Located in Massachusetts (USA), the estuary covers an area of 59.8 km², 60% of which are salt marshes dominated by *Spartina alterniflora* and *Spartina patens*. The estuary includes a primary sound that is about 1500 m wide at the inlet. Three distinct rivers discharge into the sound: the Parker, Rowley and Ipswich Rivers. The mouths of these rivers are approximately 500 m wide for the Parker River, and 300 m wide for Rowley and Ipswich Rivers.

Tidal range changes from 2.2 m to 3.6 m during neap-spring tidal modulation, with a mean tidal range of 2.9 m (LTER [Long Term Ecological Research] Tidal Station A in Fig. 1.1). The averaged depth of the sound is 3.0 m, with extensive shallow tidal flats exposed at low tide (Zhang et al. 2019). The freshwater discharge of the rivers displays strong seasonal variability. For example, the monthly mean discharge of the Parker River peaks at 2.41 m³/s in March and drops to less than 0.18 m³/s in August. Similarly, the Ipswich River discharge ranges from 12.86 m³/s to 1.19 m³/s (Fig. 1.2). The river discharge of the Rowley River is approximately 1/5 of the Parker River based on the ratio of watershed areas (Zhao et al. 2010, Hopkinson et al. 2018). The combined monthly freshwater discharge from the three rivers typically ranges from 1.40 m³/s to 15.40 m³/s but is generally negligible compared to the tidal prism (Fagherazzi et al. 2014). The tidal phase delay from the inlet to the upper bay near the mouth of the Parker River is approximately 30 minutes (Zhao et al. 2010).

Wind-wave induced bottom shear stresses act mainly on shallow tidal shoals, and are one order of magnitude smaller than the stresses triggered by tidal currents flowing in the deep channels of the sound. Analysis of bed samples shows that the fraction of silt and clay is 5.2 % in the sound and reaches 20% with finer mean grain sizes of 142 µm in the rivers (Fagherazzi et al. 2014). Sea level is rising at about 2.8 mm yr⁻¹ in this region (Claessens et al. 2006; Hopkinson et al. 2018). Hundreds of small dams present in the rivers watersheds reduce the sediment load, alter river flow dynamics, and influence both suspended matter and wetland stability in the Plum Island Estuary (Hein et al. 2012).

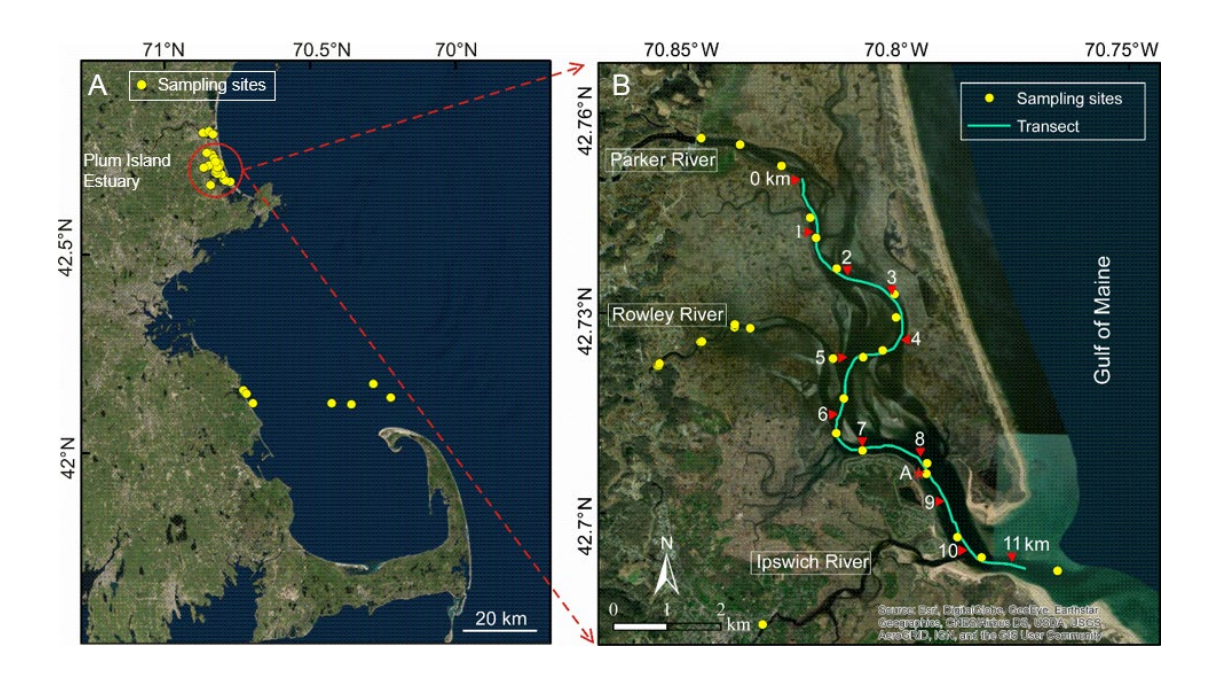


Figure 1.1 (A) Location of the Plum Island Estuary in Massachusetts, USA and 40 sampling sites. (B) Locations of the Parker, Rowley and Ipswich Rivers. Numbers of 0-11 km (red triangles) indicate distances along the thalweg of the sound (green line) from the mouth of the Parker River to the Ocean. Yellow dots indicate 26 sites sampled in 2018. The long-term observation station A is at the Ipswich Bay Yacht Club pier and belongs to PIE-LTER.

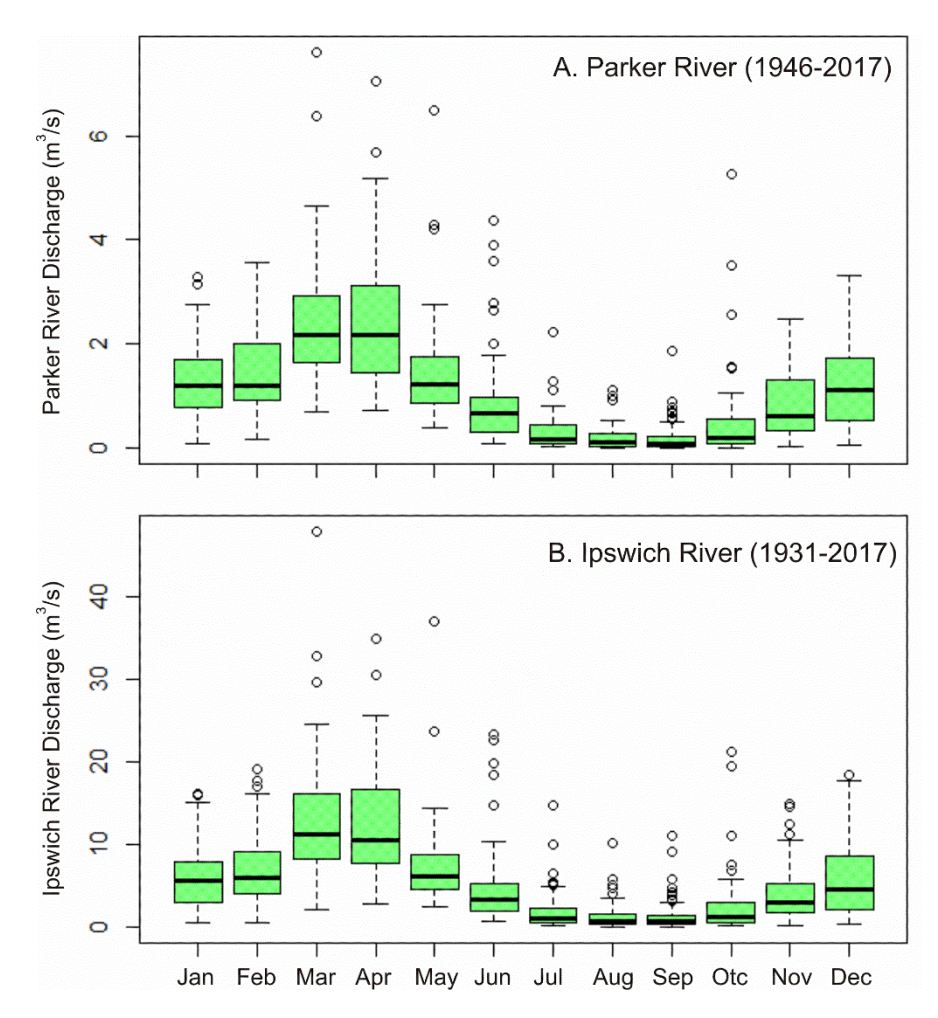


Figure 1.2 (A) Parker River monthly discharge recorded at USGS station 01101000. (B) Ipswich River monthly discharge recorded at USGS station 01102000.

1.3 Materials and methods

1.3.1 In situ measurements

A total of 40 stations were sampled in the Plum Island Estuary and in Massachusetts Bay during October and November 2017 and from May to July 2018 (Fig. 1.1, Table 1.2). Most of the samples were collected in the Plum Island Estuary and the few samples (7)

collected in Massachusetts Bay were used as ocean end-members to help improve the performance of the algorithm at low suspended sediment concentrations.

Suspended Sediment Concentration (SSC): Surface water samples (0.5 m depth) were collected using a 4-L horizontal Van Dorn sampler. The entire sample was drained in a 4-L amber high-density-polypropylene (HDPE) bottle and kept on ice in a cooler or at 4°C until analysis, usually within a few hours of sampling. Samples were analyzed for suspended sediment concentration in the laboratory following the protocol of Neukermans et al. (2012). A volume ranging 0.5 L to 2 L of sample water (depending on in situ measured turbidity) was filtered on pre-weighed GF/F glass microfiber filters with a pore size of 0.7 μm, rinsed with at least 250-mL of high-purity water (Milli-Q), and dried at 75°C for 24 h. Weights of the filter were measured using a Sartorius Cubis MSE3.6P000DM Microbalance.

Turbidity: A YSI ProDSS Multiparameter Water Quality Meter with sensors for temperature, conductivity, depth, dissolved oxygen, chlorophyll-a fluorescence, and turbidity (infrared detector, 90°, Formazin Nephelometric Unit (FNU)) was deployed at each station in the Plum Island Estuary during the May-July 2018 time period (not available for 2017 sampling). Turbidity measurements were collected with a sampling rate of 1 Hz for 1-2 min at each station, and the average was calculated after removal of outliers (any data above 2 times the standard deviation). The YSI ProDSS was also equipped with a GPS, and in some cases the YSI ProDSS was used to make underway

measurements just below the surface (0.1 - 0.2 m depth) from the bow of the boat and away from bubbles produced during the boat's movement.

Spectral remote-sensing reflectance ($Rrs(\lambda)$): The spectral remote-sensing reflectance of the water, $Rrs(\lambda)$, was measured wherever water samples for SSC were collected. Measurements were only made when water was deeper than 3 m or was attenuating enough than the bottom evidently had minimal influence on the $Rrs(\lambda)$. Two different approaches were used (Fig. 1.3). For a total of 14 stations, $Rrs(\lambda)$ was determined from vertical optical profiles of upwelling radiance and downwelling irradiance acquired with a Biospherical® Compact Optical Profiling System (C-OPS) (Morrow, 2010). The C-OPS was deployed off the side of a zodiac (Plum Island Estuary stations) or from the stern of the research vessel R/V Auk (Massachusetts Bay stations, and the optical profiles were always performed at least 20 m from the boat and on the sunny side in order to avoid the boat's shadow). The optical profiles were then used to derive $Rrs(\lambda)$ just above the surface and at 19 wavelengths from 305 nm to 780 nm (including red bands at 625 and 665 nm) using well-established protocols described in Antoine et al. (2013) and Hooker et al. (2013). At least three profiles were done at each station, and the average $Rrs(\lambda)$ for the three profiles was used. For the other 26 samples (all in Plum Island Estuary), $Rrs(\lambda)$ was determined at 1 nm spectral resolution from 350-1000 m using an ASD® Handheld-2-Pro spectrometer and following the recommended procedure described in Mobley (1999). Briefly, the handheld spectrometer was used to measure radiance (here in digital counts) from three targets at each station: 1) reflected sunlight from a Spectralon® plate

(average of ~10 measurements), 2) skylight measured at 40° from the zenith and at 135° from the Sun's azimuthal plane (average of ~10 measurements), 3) water radiance measured at an angle of 40° from Nadir and at 135° from the Sun's azimuthal plane (average of ~10 measurements). All measurements of the three targets were made within 5 mins while illumination conditions were stable (e.g., no variable cloud conditions). Note all ASD measurements were made during relatively clear-sky conditions, with occasionally some high cirrus clouds. Remote-sensing reflectance was estimated as in equation

$$Rrs(\lambda) = (L_{water} - \rho^* L_{sky}) / (\pi^* L_{spectralon} / \sigma)$$
 (1.1)

where L_{water} is the measured radiance of the water, L_{sky} is the measured skylight radiance, and ρ is the fraction of skylight reflected at the air-water interface at 40° incidence angle and with dependence on wind-speed. $L_{\text{spectralon}}$ is the measured radiance of the Spectralon plate, π is a factor to convert radiance to irradiance assuming the Spectralon plate is a Lambertian surface, and σ is the reflectance of the Spectralon plate (typically > 99%, but with some spectral dependence). In order to provide a more accurate value for ρ , wind speeds were also recorded and averaged over 1 min using a handheld vane anemometer (Mobley, 1999).

Table 1.1 Parameters of different sensors

Sensor	Band	Center Wavelength [nm]	Bandwidth [nm]	Spatial resolution (m)
Operational Land Imager (OLI)	4	654.59	37.47	30
Sentinel-2A/2B	4	665	30	10

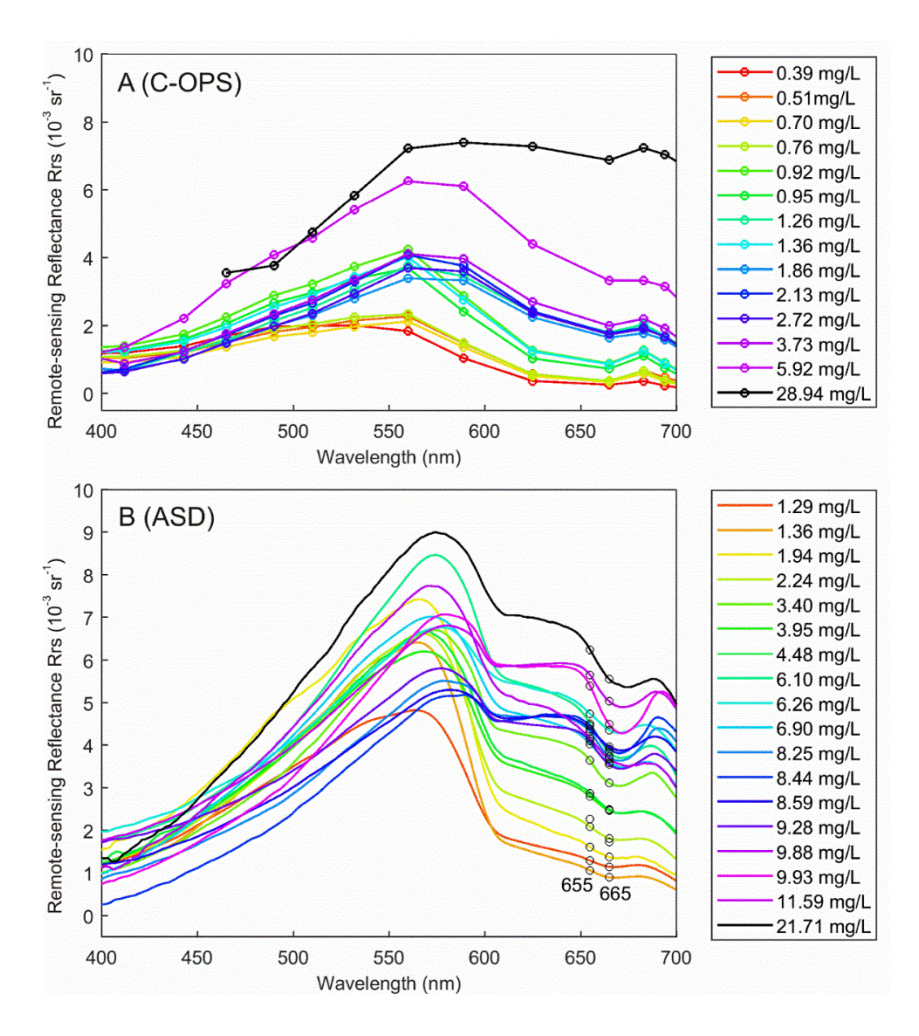


Figure 1.3 Remote-sensing Reflectance (Rrs) spectra of water samples for different SSC, measured by (A) Compact Optical Profiling System (C-OPS) and (B) ASD® Handheld-

2-Pro spectrometer. Note (A) shows all the 14 samples, (B) only show 18 samples instead of 26 samples for ease of visualization.

Table 1.2 Locations, date, SSC and Rrs (λ) measurement methods of all 40 water samples. C-OPS: Compact Optical Profiling System, is used to derive Rrs (λ) at 19 wavelengths from 305 nm to 780 nm (including red bands at 625 and 665 nm). ASD: ASD® Handheld-2-Pro spectrometer, is used to derive Rrs(λ) at 1 nm spectral resolution from 350-1000 m.

Num	Name	Date	Time	Latitude	Longitude	SSC (mg/L)	Rrs (λ) Method
1	PIE_01	11/4/2017	11:43	42.7289	-70.8457	5.92	C-OPS
2	PIE_02	11/4/2017	12:19	42.7314	-70.8345	2.13	C-OPS
3	PIE_03	11/4/2017	12:47	42.7266	-70.8156	1.26	C-OPS
4	PIE_04	11/4/2017	13:08	42.7142	-70.8145	1.86	C-OPS
5	PIE_05	11/4/2017	13:36	42.7078	-70.7939	2.72	C-OPS
6	PIE_06	11/4/2017	14:06	42.6973	-70.7866	3.73	C-OPS
7	PIE_07	11/4/2017	15:06	42.7248	-70.8553	28.94	C-OPS
8	NI01	10/16/2017	11:00	42.1678	-70.7039	0.92	C-OPS
9	NI02	10/16/2017	12:15	42.1601	-70.6946	1.36	C-OPS
10	NI03	10/16/2017	13:20	42.1366	-70.6719	0.95	C-OPS
11	SSB01	10/18/2017	14:30	42.1902	-70.2651	0.76	C-OPS
12	SSB02	10/18/2017	13:19	42.1563	-70.2062	0.39	C-OPS
13	SSB03	10/18/2017	11:51	42.1378	-70.3383	0.51	C-OPS
14	SSB04	10/18/2017	10:30	42.1395	-70.4058	0.70	C-OPS
15	PIE_061218_S01	6/12/2018	9:26-9:32	42.7619	-70.83772	21.71	ASD
16	PIE_061218_S02	6/12/2018	10:01-10:05	42.7585	-70.82822	9.88	ASD
17	PIE_061218_S03	6/12/2018	10:40 -10:44	42.7467	-70.82003	4.48	ASD
18	PIE_061218_S04	6/12/2018	11:11-11:15	42.7376	-70.802	1.94	ASD
19	PIE_061218_S05	6/12/2018	11:38-11:43	42.7337	-70.80152	1.02	ASD
20	PIE_062118_S01	6/21/2018	9:51-9:56	42.6921	-70.76372	1.36	ASD
21	PIE_062118_S02	6/21/2018	10:25-10:38	42.694	-70.781	1.29	ASD
22	PIE_062118_S03	6/21/2018	10:58-11:10	42.7095	-70.79384	2.24	ASD
23	PIE_062118_S04	6/21/2018	11:28-11:42	42.7114	-70.8085	3.95	ASD

24	PIE_062118_S05	6/21/2018	12:08-12:17	42.72	-70.813	6.90	ASD	
25	PIE_062718_S01	6/27/2018	15:12-15:55	42.7282	-70.80443	6.10	ASD	
26	PIE_062718_S02	6/27/2018	15:45-15:55	42.7315	-70.83808	6.26	ASD	
27	PIE_062718_S03	6/27/2018	16:11-16:21	42.7252	-70.85494	8.59	ASD	
28	PIE_070318_S01	7/3/2018	8:15-8:19	42.7249	-70.85501	8.44	ASD	
29	PIE_070318_S02	7/3/2018	8:37-8:39	42.729	-70.84537	8.25	ASD	
30	PIE_070318_S03	7/3/2018	8:51-8:54	42.7319	-70.83803	9.93	ASD	
31	PIE_070318_S04	7/3/2018	9:16-9:18	42.727	-70.80878	3.40	ASD	
32	PIE_070318_S05	7/3/2018	9:53-9:55	42.75	-70.82147	11.59	ASD	
33	PIE_070318_S06	7/3/2018	10:11-10:14	42.7417	-70.81526	9.28	ASD	
34	PIE_071118_S01	7/11/2018	9:22-9:23	42.682	-70.83028	7.33	ASD	
35	PIE_071118_S03	7/11/2018	10:26-10:27	42.7252	-70.85492	6.77	ASD	
36	PIE_071118_S04	7/11/2018	10:53-10:55	42.7629	-70.84653	11.90	ASD	
37	MR_071918_S01	7/19/2018	10:51-10:54	42.8127	-70.85472	7.65	ASD	
38	MR_071918_S02	7/19/2018	11:09-11:11	42.8135	-70.86009	7.67	ASD	
39	MR_071918_S03	7/19/2018	11:31-11:33	42.817	-70.84015	7.37	ASD	
40	MR_071918_S04	7/19/2018	11:57-11:59	42.8095	-70.82726	8.11	ASD	

1.3.2 Development of local empirical algorithms for the retrieval of SSC from OLI and MSI

The paired in situ measurements of SSC and $Rrs(\lambda)$ described above were used to derive simple empirical algorithms that can be implemented on OLI and MSI imagery. It is well established that the Rrs in the red or near-infrared region can be used as a sensitive predictor of SSC in waters where suspended sediments are important drivers of optical variability (Nechad et al. 2010, Giardino et al. 2010, Vanhellemont et al. 2014, Fichot et al. 2016, Constantin et al. 2018). Not surprisingly, Rrs in the red region was also strongly and non-linearly related to SSC in this system (Fig. 1.4). In order to develop algorithms specifically applicable to the Landsat-8 OLI and the Sentinel-2A/B MSI, the relative

spectral responses of the OLI and MSI red bands were used to calculate spectrally weighed remote-sensing reflectance from the hyperspectral *in situ* $Rrs(\lambda)$ measured with the ASD. As described in Pahlevan et al. (2017a), the spectrally weighed remote-sensing reflectance over the center wavelength $\lambda_c = 655$ nm (OLI) and $\lambda_c = 665$ nm (MSI) was calculated as in equation (1.2):

$$\overline{R_{rs}}(\lambda_c) = \frac{\sum_{1}^{n} R_{rs}(\lambda_i) RSR(\lambda_i)}{\sum_{1}^{n} R_{rs}(\lambda_i)}$$
(1.2)

where $\overline{R_{rs}}(\lambda_c)$ is the remote-sensing reflectance spectrally weighed over the OLI/MSI broad red band, $R_{rs}(\lambda_i)$ is the hyperspectral remote-sensing reflectance (1-nm spectral resolution) measured in situ using the ASD. $RSR(\lambda_i)$ is relative spectral response of the OLI/MSI over the broad red band, with n = 67 for 1-nm resolution data over the range 625-691 nm (OLI), n = 39 over the range 646-684 nm (Sentinel-2A MSI), and n=40 over the range 646-685 nm (Sentinel-2B MSI). This spectral weighing procedure was applied to the 26 measurements made with the ASD, but it could not be applied to the 14 samples measured with the C-OPS considering the instrument only provides measurements at 19 wavelengths. In this case, the Rrs(665) measured directly from the C-OPS was used as an estimate of the MSI red-band Rrs, and the Rrs(655) estimated from linear interpolation of Rrs(625) and Rrs(665) measured directly with the C-OPS used as an estimate of the red-band OLI Rrs. However, a simple comparison of Rrs at discrete wavelength and spectrally weighed Rrs using the ASD data revealed that this limitation only introduced a +/- 4.06% uncertainty in the C-OPS derived MSI and OLI red-band Rrs and had very limited impact on the parameterization of the algorithms (Fig. 1.5 and Table 1.2).

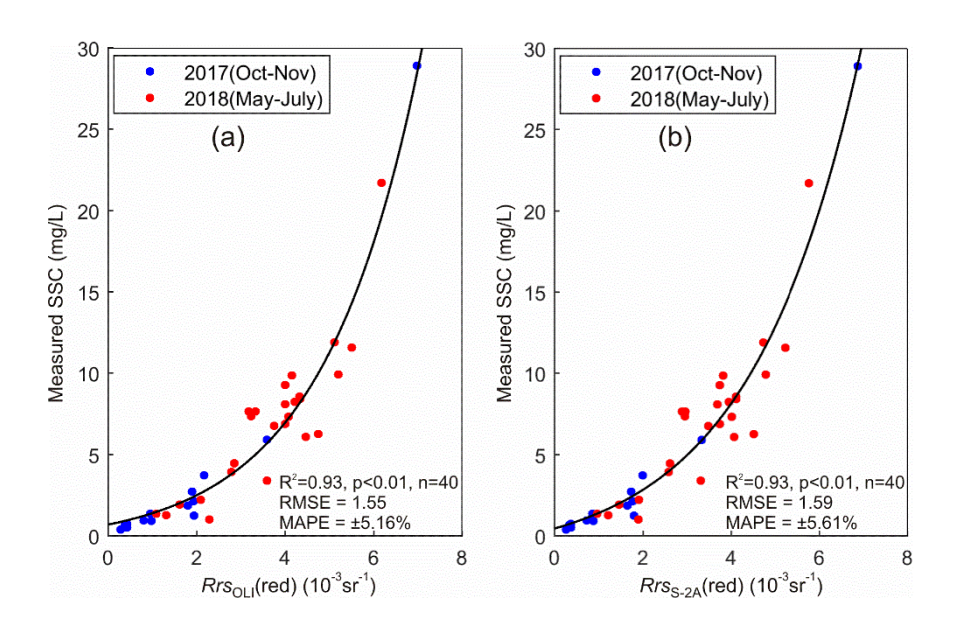


Figure 1.4 Measured SSC as a function of measured Remote-sensing reflectance (combined 14 discrete remote-sensing reflectance and 26 spectrally weighed Remote-sensing reflectance) at 655 nm (*Rrs*_{OLI}(red)) for Landsat-8 OLI (a), 665 nm (*Rrs*_{S-2A} (red)) for Sentinel-2A MSI (b) sensors based on 40 water samples (Fig. 1.1). RMSE represents root mean square error and MAPE mean absolute percentage error (Eq.1.6).

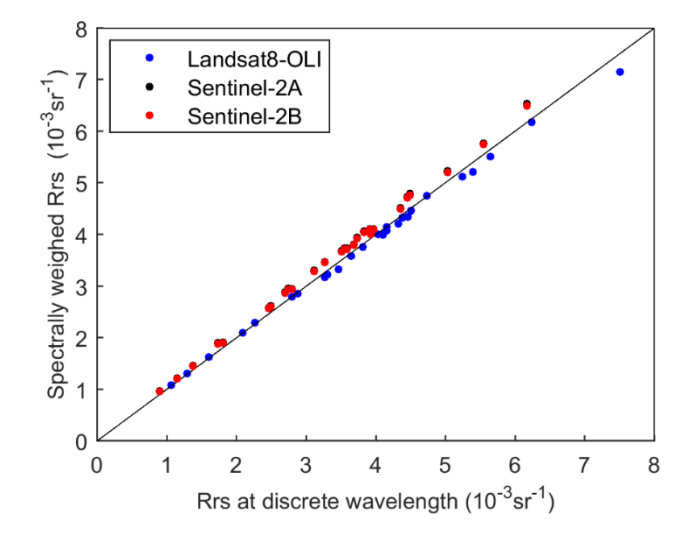


Figure 1.5 Difference between Remote-sensing Reflectance Rrs, at a discrete wavelength corresponding to the center of the red band of the OLI (655 nm) and MSI (665 nm), and the Rrs spectrally weighed over the corresponding broad red band of these sensors. The difference highlights an average difference of \pm 4.06%. Data were simulated here using the 26 samples collected with the ASD Handheld-2 Pro spectrometer.

A combination of 26 spectrally-weighed *Rrs* and 14 discrete *Rrs* were thus used to develop the three sensor-specific algorithms based on exponential fits of the measured SSC on the measured red-band *Rrs* (Fig. 1.4) and shown in Eqs. 1.3 to 1.5:

$$SSC_{OLI} = 1.2158 * exp(453.87 * Rrs_{OLI}(red)) - 0.5159$$
 (1.3)

$$R^2$$
 = 0.931, p-value <<0.001, RMSE = 1.55, Mean Absolute Percentage Error (MAPE) = (±5.16%)

$$SSC_{MSI-S2A} = 1.9318 * exp(401.15 * Rrs_{S2A}(red)) - 1.4729$$
 (1.4)

$$R^2 = 0.927$$
, p-value $<< 0.001$, $RMSE = 1.59$, $MAPE = (\pm 5.61\%)$

$$SSC_{MSI-S2B} = 2.0107 * exp(396.04 * Rrs_{S2B}(red)) - 1.5804$$
 (1.5)

$$R^2 = 0.927$$
, p-value <<0.001, RMSE = 1.59, MAPE = (±5.63%)

The indicator of MAPE is calculated as:

$$MAPE = \pm \frac{1}{N} \sum_{i=1}^{N} \left| \frac{y_{i-} y_{i}'}{y_{i}} \right|$$
 (1.6)

Where y_i and y_i^\prime indicate measured and modelled SSC respectively, and N is total number of observations.

SSColl, SSCs24 and SSCs28 are the suspended sediment concentrations to be derived from the remote-sensing reflectance over the broad red band of the Landsat-8 OLI (Rrsoll (red)), Sentinel-2A MSI (Rrs_{S-2A} (red)) and Sentinel-2B MSI (Rrs_{S-2B} (red)) sensors respectively. These simple algorithms show that the red-band Rrs explains 93% of the variance in SSC across a range of 1 to 30 mg L⁻¹, which is representative of the range of SSC typically measured over the past 15-years (Hopkinson et al., 2018). The algorithms facilitate the retrieval of SSC within \pm 5.47% of the measured values. The observed scatter in the relationships between red-band Rrs and SSC can be caused by several factors: 1) uncertainties in the measurements of SSC and Rrs, 2) differences in particle size, shape, and type which can influence the specific inherent optical properties of the suspended particles (e.g., volume scattering phase function, and mass-specific absorption coefficient), 3) influence of bottom reflectance in some of the shallower waters sampled (e.g., during low tide), and to a lesser extent 4) independent variations in chromophoric dissolved organic matter which can contribute to some variability in Rrs even in the red.

1.3.3 Processing of OLI and MSI imagery and implementation of the algorithms

Level-1 data from Landsat-8 OLI, Sentinel-2A MSI, and Sentinel-2B MSI were obtained

from the USGS Earth Explorer website (https://earthexplorer.usgs.gov) and were

atmospherically corrected using the NASA SeaDAS v.7.5.1 comprehensive software

package for the processing, display, analysis, and quality control of ocean color data. Briefly, the *l2gen* processor was used to generate Level-2 mapped rasters of the red-band *Rrs* from the Level-1 top-of-atmosphere calibrated radiances using the standard multi-scattering and iterative near infrared (NIR) model of Bailey et al., (2010) and the vicarious gains of Pahlevan et al. (2017b). A total of 46 mostly-clear scenes of red-band *Rrs* were thus generated, including 24 scenes from Landsat-8 at 30-m spatial resolution, 14 from Sentinel-2A at 10-m spatial resolution, and 8 from Sentinel-2B also at 10-m spatial resolution. The sensor-specific algorithms displayed in Eqs. 1.3-1.5 were then applied to their corresponding scenes to produce SSC maps.

Large portions of the Plum Island Estuary consists of shallow areas. In order to avoid significant contamination by bottom reflectance, only remotely sensed data collected over the center of the main channel were used in this study. Bottom depth along the transect increased progressively from a minimum of 2.5 m in the more turbid upstream reaches of the estuary (from marker 0 to 1-km) to more than 10-m near the mouth of the estuary (Fig. 1.6). A simple quantitative analysis was done to assess the potential influence of bottom reflectance on the remotely sensed Rrs(665). It revealed that bottom reflectance unlikely affected the observed remotely sensed Rrs(665) along the transect, with the exception of a short and shallow section of the transect located between the 8.25 and 8.75-km markers, where a combination of clearer waters and a bottom depth of < 5 m likely led to a significant contribution of bottom reflectance. However, a simple comparison indicated that the apparent increase in Rrs(665) due to bottom reflectance observed between the

8.25 and 8.75-km markers only caused an average increase of 0.5% in the transect-averaged SSC and was therefore not considered an issue for the purpose of this study.

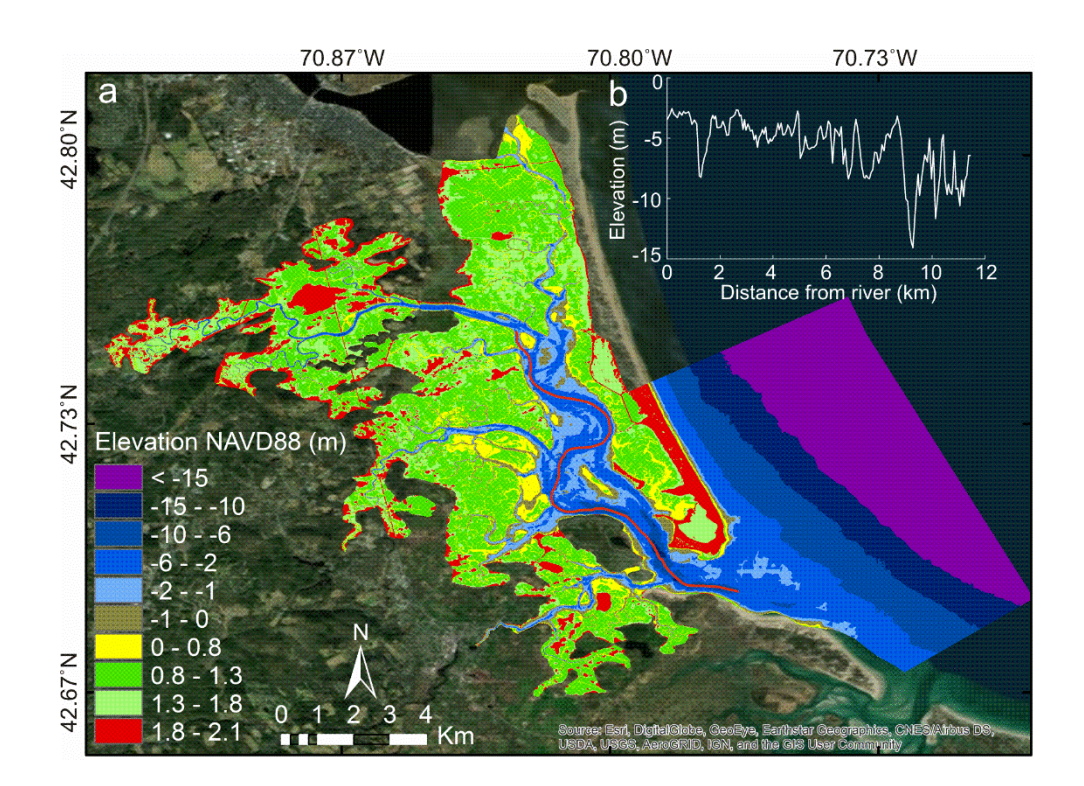


Figure 1.6 Elevation (NAVD88) of the Plum Island Estuary: (a) Map derived from a combination of LIDAR and GPS bathymetry measurements provided by LTER-PIE (https://pie-lter.ecosystems.mbl.edu/data), (b) elevation along the thalweg of the sound (red line) from the mouth of the Parker River (Marker 0 km) to the mouth of the esuatry (Marker 11.3 km).

1.3.4 Potential influence of bottom reflectance on the remotely sensed Rrs(665)

A simple quantitative analysis was done to estimate the approximate potential contribution of bottom reflectance on the average remotely-sensed *Rrs* along the thalweg

transect. In this analysis, the $Rrs^B(665)$ contributed by the bottom reflectance of incident irradiance was estimated using Eq. 1.7

$$Rrs^{B}(665) \cong \frac{L_{W}^{B}(665)}{E_{d}(0^{+},665)}$$
 (1.7)

where the $L_W^B(665)$ is the water-leaving radiance at 665 nm contributed by the bottom reflectance of the irradiance incident above the air-water interface at 665 nm, $E_d(0^+,665)$. Here, $L_W^B(665)$ can be approximated using Eq. (1.8)

$$L_W^B(665) \cong \left(\frac{1}{\pi}\right) * 0.96 * E_d(0^+, 665) * \exp(K_d(665) * z) * \exp(K_u(665) * z) * R_B * 0.54$$
 (1.8)

where K_d (665) is the diffuse attenuation of downward irradiance at 665 nm, K_u (665) is the diffuse attenuation of upwelling irradiance at 665 nm, z is the bottom depth (negative value), R_B is the bottom irradiance reflectance, the $1/\pi$ factor is used to convert water-leaving reflectance to remote-sensing reflectance assuming an isotropic upward light field, and the 0.54 and 0.96 factors account for reflection of upwelling radiance and downwelling irradiance, respectively, at the air-water interface. In most cases, K_d and K_u are very close in value (Howard and Morel, 2012), such that Eq. (1.8) can be simplified to:

$$L_W^B(665) \cong \left(\frac{1}{\pi}\right) * 0.96 * E_d(0^+, 665) * \exp(K_d(665) * z * 2) * R_B * 0.54$$
 (1.9)

Inserting Eq. (1.9) into Eq. (1.7) yields Equation (1.10):

$$Rrs^{B}(665) \cong \left(\frac{1}{\pi}\right) * 0.96 * \exp(K_d(665) * z * 2) * R_B * 0.54$$
 (1.10)

Here, $Rrs^B(665)$ was calculated along the transect (Fig.1.7) using Eq. (1.10) and the following data:

1) Bottom depth z along the transect (Fig. 1.7A), extracted from the bathymetry data (see Fig. 1.6).

- 2) A linear increase of bottom irradiance reflectance $R_B(665)$ ranging from 0.1 in the muddy sediment upstream to 0.5 in for the more sandy sediments near the mouth of the estuary (Fig. 1.7B), based on reported data (Volpe, 2011) and reflecting the general gradient of bottom sediment type along the transect (Fagherazzi et al., 2014).
- 3) Values of $K_d(665)$ measured across a representative range of water types in the Plum Island Estuary using a Biopherical C-OPS (See Methods) ranged from $\sim 0.55 2 \text{ m}^{-1}$ and were found to be strongly linearly correlated ($R^2 > 0.90$, n = 45) with SSC measured on samples acquired coincidently *in situ*. This strong relationship is not surprising considering that backscattering by particles is the main factor influencing K_d at 665 nm besides the constant absorption by water. This relationship, $K_d(665) = 0.0845*SSC + 0.4934$, was thus used to estimate an average $K_d(665)$ transect from the average of all remotely sensed SSC transects used in this study (Fig. 1.7C).

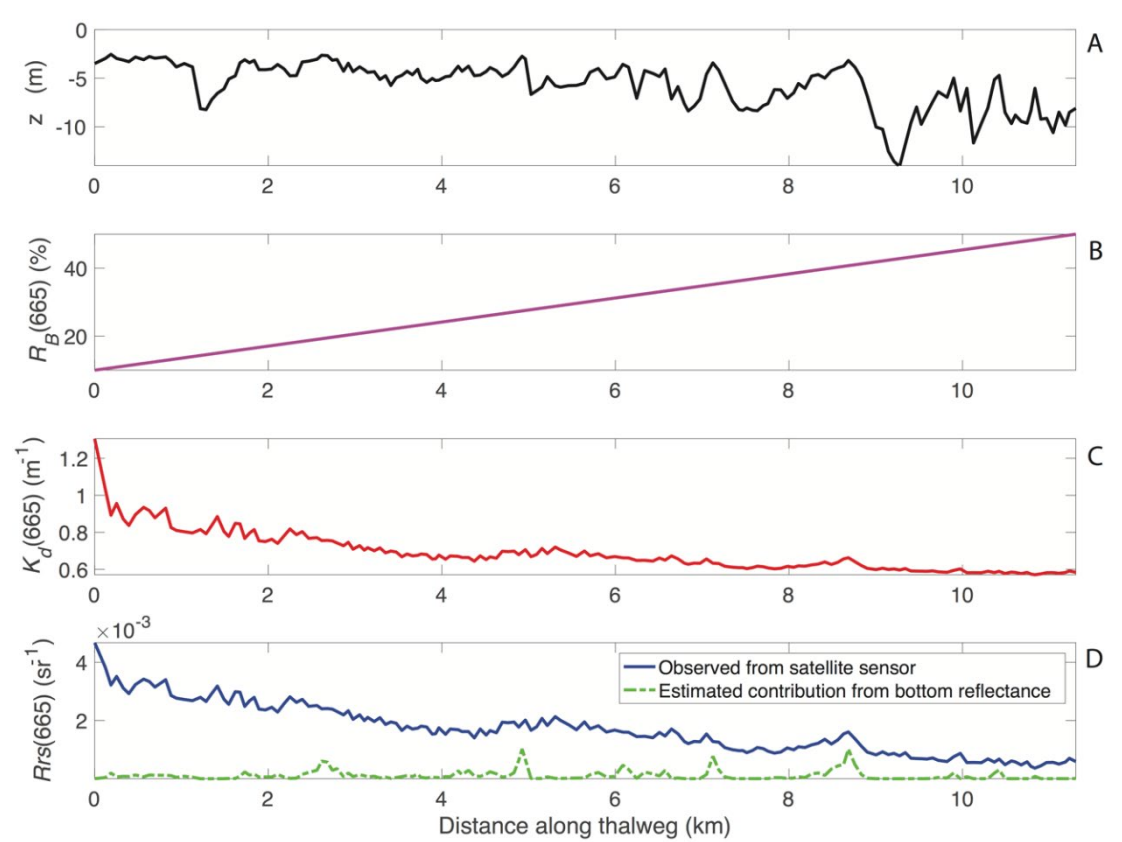


Figure 1.7 Potential contribution of bottom reflectance to the average Rrs(665) observed along the thalweg of the main channel of the Plum Island Estuary, along with the variables used to calculate it. (A) Bottom depth z from bathymetry. (B) Assumed bottom irradiance reflectance (C) $K_d(665)$ estimated from the average distribution of SSC along the transect. (D) Average remotely sensed Rrs(665) from all scenes, and potential contribution from bottom reflectance.

The lack of correspondence between the transect of remotely sensed Rrs(665) and the calculated contribution from bottom reflectance (Fig.1.7D) indicates that the bottom reflectance contributed minimally to the observed patterns of Rrs(665) variability, except for a shallow 0.5-km section of the transect located between markers 8.25 and 8.75 km, where clearer waters (lower $K_d(665)$ values) and shallow bottom likely contributed to an apparent increase in remotely sensed Rrs(665).

1.3.5 Hydrodynamic and meteorological analysis

Water level, wind conditions, and river discharge data were collected at the same instant of each satellite image. The LTER-PIE services a fixed meteorological station at the Ipswich Bay Yacht Club pier (see location A in Fig. 1.1), recording water level, wind speed, and direction every 15 minutes. Daily river discharge data for the Parker River and Rowley River are available at the USGS stations 0110100 and 01102000 respectively. Tidal discharge is an important parameter for sediment dynamics. In fact when the tidal discharge is maximum, usually near mean sea level for mudflats, water velocities at the bottom are high, leading to high bottom shear stresses and sediment resuspension, thus increasing SSC. An estimate of the temporal variations in tidal discharge in a system is quite complex (see Kearney et al. 2017), and usually requires a high resolution numerical

model (e.g. Zhang et al. 2019) or intensive field measurements (Fagherazzi and Priestas 2010). Here we use the temporal variation in water level dh/dt as a proxy for tidal discharge, with positive values indicating flood direction. This approximation is based on the tub model of Boon (1975), who showed that for continuity in a tidal system a change in water level requires an input/output of a volume of water in the system. To a first approximation, we can write (Boon 1975):

$$Q = A \frac{dh}{dt} \tag{1.11}$$

Where Q is the tidal discharge entering the system, A is the flooded area of the bay, which can be considered constant to a first-order approximation, and dh/dt the variation in water level triggered by the tide.

This model does not account for the variability in flooded area due, for example, to wetting and drying of marshes or the propagation of the tide in the system, which causes a spatially-variable dh/dt in the bay (Fagherazzi et al. 2008). However, this simple approximation correctly captures the low flow at slack water, the discharge peak near MSL, and neap/spring modulations in tidal discharge. More importantly, temporal variations in water level dh/dt can be readily computed from a tidal gauge without the need of bathymetric data, and it is therefore ideal ancillary data for remote sensing images.

The 46 scenes used in this manuscript cover the entire tidal cycle of flood and ebb tides and high and low water levels. In Figure 1.8 we plot the average sediment concentration

as a function of water level and rate of water level change, *dh/dt*. The rate of water level change is a proxy for tidal flow, and it is positive during flood and negative during ebb (Fagherazzi et al. 2008). Our measurements span low and high tide as well as low and high flow, although there was a slight bias towards high flow conditions during flood (high rates of water-level change) when the water level is around zero (Fig. 1.8). The wind speed ranges from 0.97 to 11.81 m/s, and river discharge of Parker River ranges from 0.01 to 6.17 m³/s (Table 1.4). These 46 scenes cover entire tidal cycle, normal wind conditions (Fagherazzi et al. 2014) and a typical range of river discharge (Fig. 1.2), thus providing a representative database to capture the main drivers contributing to variations of SSC in the study area.

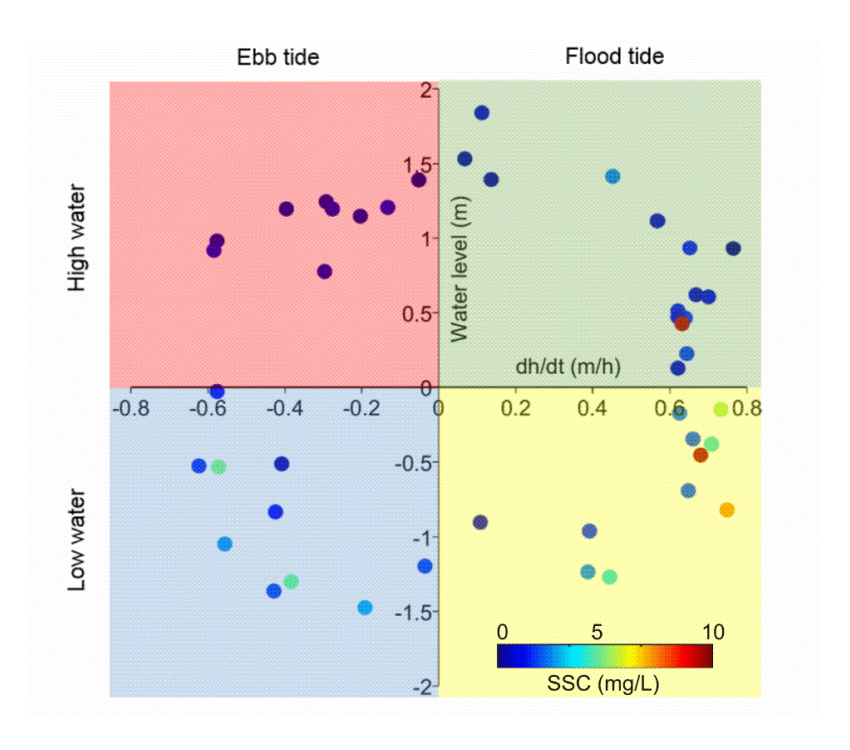


Figure 1.8 Relationship between in-situ measured water level, temporal variations in water level dh/dt at Ipswich Bay Yacht Club pier (see location A in Fig. 1.1) and transect

averaged SSC (n=46). *dh/dt* is a proxy for tidal flow and positive values indicate flood tide. The data highlight that the remote-sensing data cover a representative range of tidal conditions typically encountered at the Plum Island Estuary.

1.4 Results

1.4.1 Distribution of SSC as a function of river discharge, wind and tides

Table 1.3 Hydrodynamic and meteorological parameters of representative SSC maps shown in Fig. 1.9, 1.10.

Figure	Date	Water level (m)	LTER dh/dt (m/h)	Wind speed (m/s)	Wind direction (°)	Parker discharge (m3/s)	SSC (mg/L)	Dominated factor
1.9a,1.10a	10/12/2014	-0.35	0.66	3.19	331.80	0.01	2.20	High tidal flow
1.9b,1.10a	10/5/2017	1.39	0.14	3.11	290.40	0.24	0.51	Low tidal flow
1.9c,1.10b	10/20/2017	1.12	0.57	6.58	303.10	0.01	0.97	Flood tide
1.9d,1.10b	12/1/2017	0.98	-0.58	6.98	308.40	0.42	0.52	Ebb tide
1.9e,1.10c	4/3/2014	-0.45	0.68	3.07	57.50	6.17	9.87	High discharge
1.9f,1.10c	3/18/2014	0.46	0.64	2.49	62.50	1.83	1.72	Low discharge
1.9g,1.10d	3/11/2017	1.39	-0.05	9.93	272.00	1.14	0.40	High wind speed
1.9h,1.10d	7/5/2013	0.78	-0.30	2.05	312.10	3.20	0.77	Low wind speed
1.9i,1.10e	3/26/2018	-0.53	-0.57	7.33	26.73	1.64	4.08	Northeast wind

 $1.9j, 1.10e \quad 2/6/2017 \quad -0.53 \quad -0.62 \quad 7.10 \quad 313.20 \quad 1.16 \qquad 1.82 \qquad \text{Northwest} \\ \text{wind}$

Possible hydrodynamic and meteorological controls on water surface SSC include tidal currents, river discharge, and wind-generated waves. To qualitatively illustrate these different controls, we selected pairs of images in which only one hydrodynamic or meteorological variable significantly varies (Table 1.3). The sole influence of tidal current magnitude on SSC, under similar conditions of river discharge, wind speed, and wind direction was showed in the SSC maps derived from the OLI and MSI (Fig. 1.9a, b). The sole influence of tidal current direction (Fig. 1.9c, d), river discharge (Fig. 1.9e, f), wind speed (Fig. 1.9g, h) and wind direction (Fig. 1.9i, j) were also illustrated in these high-resolution maps.

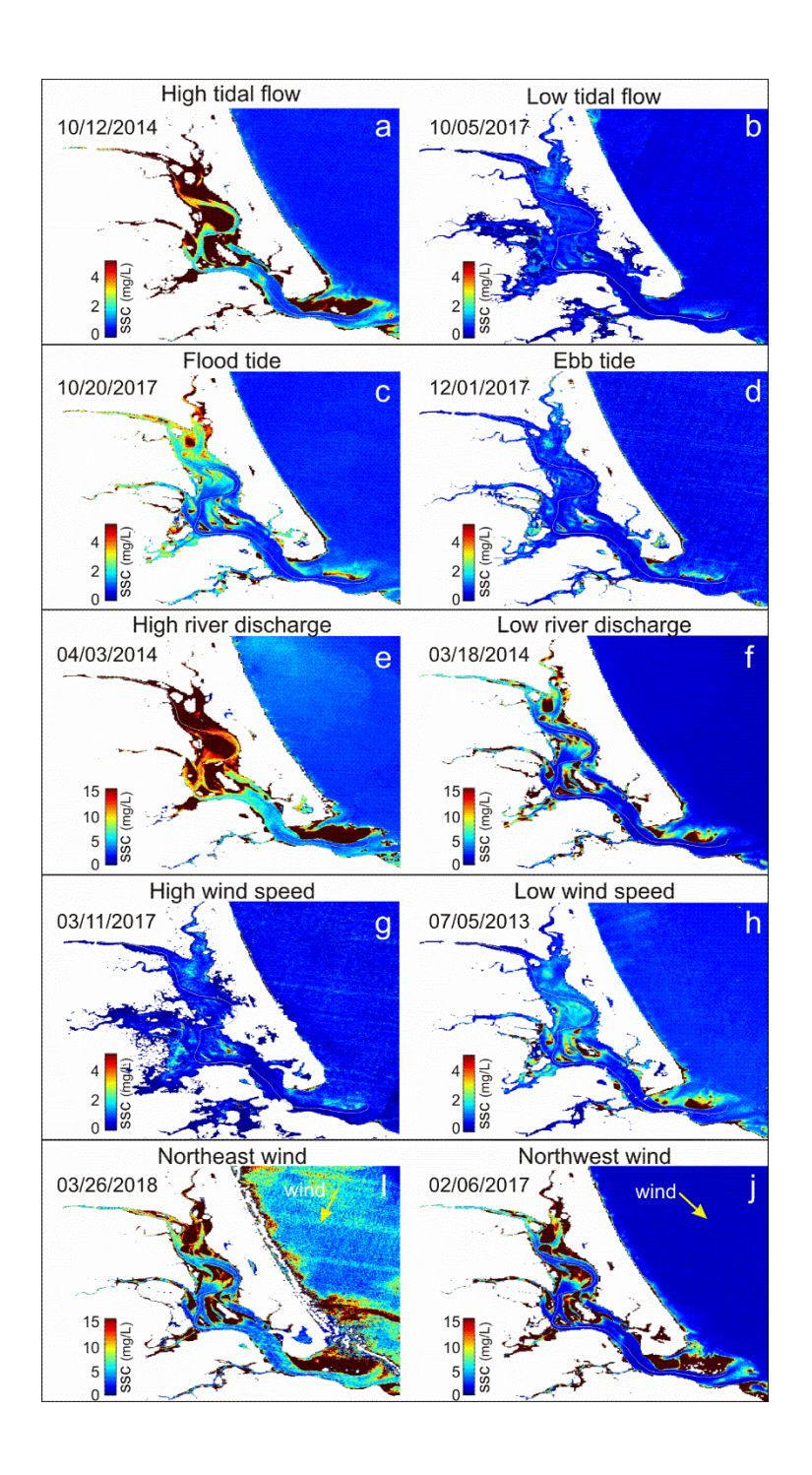


Figure 1.9 Spatial distribution of SSC as a function of different hydrodynamic and meteorological factors: tidal current magnitude (a, b); tidal current direction (c, d); river discharge (e, f); wind speed (g, h) and wind direction (i, j).

The SSC in the upper bay increased by an order of magnitude when the water-level rate of change (dh/dt) increased from 0.14 m/h (October 5, 2017) to 0.66 m/h (October 12, 2014) (Fig. 1.9a, b and Fig. 1.10a). This is because a fast increase in water level led to higher tidal velocities in the bay, resuspending bottom sediments and increasing SSC (Fagherazzi et al. 2012). SSC was 1-2 times larger during flood than ebb although winds and freshwater discharges were slightly stronger during ebb (Fig. 1.10b). An extreme river flood of the Parker River and associated sediment plume was detected on April 3, 2014, with a river discharge of 6.17 m³/s (Fig. 1.9e,f). The river flood caused a SSC 4-5 times larger than the average along the entire bay (Fig. 1.10c). Values of SSC in March 11, 2017 with a wind speed of 9.93 m/s are slightly lower than values of SSC in July 5, 2013 with a wind speed of 2.05 m/s (Fig. 1.10d). This result indicates that wind speed might have a weak control on suspended sediments; we therefore suggest that variations in water level and river discharge are more important for SSC dynamics. A Nor'easter storm in March 26, 2018 (Fig. 1.9i, j) was also captured in our analysis, with wind speed of 7.33 m/s and wind direction of 26°. We compared this event with an image taken on February 6, 2017 with similar wind speed of 7.31 m/s but approximately reversed wind direction of 313°. Strong wind waves caused by the Nor'easter storm contributed to more sediment resuspension especially in the shallower upper bay and along the shoreline (Fig. 1.9i, j and Fig. 1.10e).

We calculated averaged SSC along the thalweg of all scenes in different seasons and grouped them by flood and ebb directions. SSC generally decreased seaward and was

significantly larger during flood than during ebb in the upper bay (Fig. 1.11a). The SSC presented seasonal differences, with the spring season featuring the largest SSC (Fig. 1.11b) because of higher river discharge (see Fig. 1.2 and Table 1.4). Higher SSC occurred during flood in both spring and fall seasons (Fig. 1.11b, d), while in summer and winter the magnitude of SSC in flood was comparable to that in ebb (Fig. 1.11c, e). We conclude that SSC during flood tide was generally higher than during ebb tide, and the reasons will be examined in following sections.

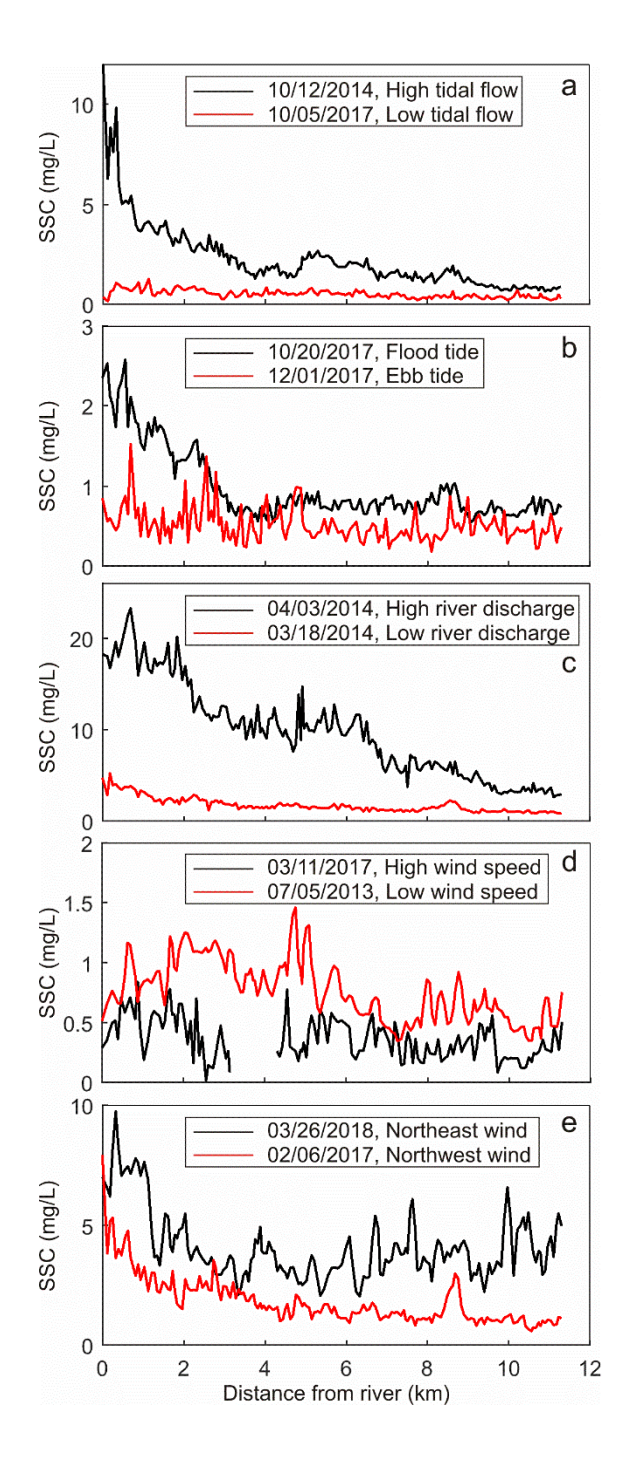


Figure 1.10 Distribution of SSC along the main channel thalweg (see thalweg location in Fig. 1.1) showcasing, in each case, the dominant effect of a single factor: (a) tidal current magnitude; (b) tidal current direction; (c) river discharge; (d) wind speed; and (e) wind direction.

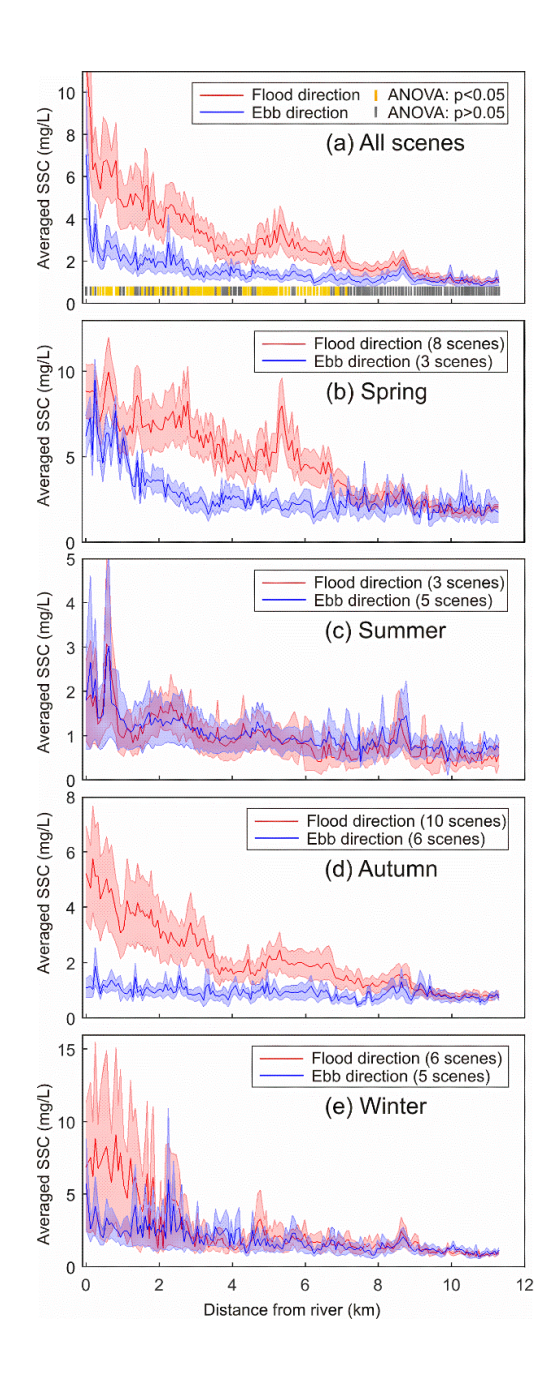


Figure 1.11 Seasonal averaged SSC along the main channel thalweg in spring (a), summer (b), autumn (c), and winter (d) grouped by flood and ebb directions. Shaded area around the lines indicate the 95% confidence interval. The yellow colored bar at the bottom of (a) indicates where the SSC values in flood are significantly higher than SSC values in ebb (*p*-value<0.05 in analysis of variance ANOVA).

Table 1.4 Hydrodynamic and meteorological conditions of 46 scenes used.

C	D-4-	C	Water	dh/dt	Wind	Wind	Parker	T: -1-	SSC
Scene Num	Date	Sensors	level	an/at (m/h	speed	wind directio	discharg	Ipswich discharg	(mg/L
			(m))	(m/s)	n (°)	$e (m^3/s)$	$e (m^3/s)$)
1	4/4/2013	OLI	-1.05	-0.56	5.70	313.20	1.47	8.38	2.84
2	7/5/2013	OLI	0.78	-0.30	2.05	312.10	3.20	11.33	0.77
3	8/22/2013	OLI	0.93	0.76	2.11	266.90	0.04	0.84	0.29
4	9/7/2013	OLI	0.62	0.67	2.42	260.10	0.02	0.50	0.95
5	9/23/2013	OLI	-0.17	0.62	6.15	310.50	0.09	0.54	2.53
6	3/18/2014	OLI	0.46	0.64	2.49	62.50	1.83	9.85	1.72
7	4/3/2014	OLI	-0.45	0.68	3.07	57.50	6.17	37.66	9.87
8	8/9/2014	OLI	1.24	-0.29	1.43	21.10	0.04	1.04	0.62
9	9/26/2014	OLI	0.51	0.62	3.41	21.40	0.01	0.18	1.68
10	10/12/2014	OLI	-0.35	0.66	3.19	331.80	0.01	0.36	2.20
11	1/16/2015	OLI	-0.03	-0.58	2.11	232.80	0.91	4.53	1.32
12	8/28/2015	OLI	1.20	-0.28	2.26	53.60	0.11	0.46	0.79
13	4/24/2016	OLI	0.22	0.64	3.12	76.70	0.77	3.85	2.10
14	5/10/2016	OLI	-0.82	0.75	2.91	310.60	0.78	5.15	7.48
15	11/2/2016	OLI	0.47	0.62	3.08	296.40	0.01	1.89	1.18
16	11/18/2016	OLI	-0.15	0.73	5.47	338.60	0.08	2.15	5.52
17	2/6/2017	OLI	-0.53	-0.62	7.10	313.20	1.16	3.77	1.82
18	3/11/2017	S2A	1.39	-0.05	9.93	272.00	1.14	5.13	0.40
19	8/1/2017	OLI	-0.51	-0.41	2.24	26.40	0.08	1.95	0.52
20	9/27/2017	S2A	-0.90	0.11	2.06	155.80	0.02	0.16	0.78
21	10/4/2017	OLI	1.21	-0.13	2.26	260.80	0.01	0.14	0.93
22	10/5/2017	S2B	1.39	0.14	3.11	290.40	0.24	0.14	0.51
23	10/10/2017	S2A	-0.69	0.65	6.97	297.60	0.08	0.19	2.18
24	10/12/2017	S2B	-1.20	-0.04	5.77	32.00	0.02	0.13	2.02
25	10/17/2017	S2A	1.20	-0.40	0.97	23.30	0.01	0.11	0.55
26	10/20/2017	OLI	1.12	0.57	6.58	303.10	0.01	0.09	0.97
27	12/1/2017	S2B	0.98	-0.58	6.98	308.40	0.42	2.12	0.52
28	12/7/2017	OLI	-0.38	0.71	4.21	265.70	0.46	1.63	4.49
29	12/11/2017	S2B	-0.83	-0.42	1.93	273.80	0.63	1.77	1.40
30	12/16/2017	S2A	1.15	-0.20	4.13	288.70	0.42	1.94	0.59
31	12/21/2017	S2B	0.13	0.62	6.39	292.60	0.33	1.55	1.01
32	1/18/2018	S2A	0.93	0.65	2.83	287.40	2.04	7.39	1.53
33	1/25/2018	S2A	-1.30	-0.38	11.81	282.60	1.22	5.32	4.33

34	2/17/2018	S2A	0.61	0.70	2.37	58.48	1.75	10.51	1.16
35	2/27/2018	S2A	0.92	-0.58	6.96	295.40	1.80	9.00	1.01
36	3/1/2018	S2B	1.84	0.11	3.14	41.42	1.57	8.50	0.89
37	3/19/2018	S2A	0.42	0.63	10.37	290.90	1.98	12.37	9.64
38	3/26/2018	S2A	-0.53	-0.57	7.33	26.73	1.64	9.03	4.08
39	3/31/2018	S2B	1.42	0.45	4.29	303.80	1.82	8.92	2.66
40	4/5/2018	S2A	-1.27	0.44	6.38	302.40	2.10	9.68	4.25
41	4/23/2018	S2B	-1.36	-0.43	2.37	108.40	2.44	14.55	1.28
42	4/28/2018	S2A	1.53	0.07	2.72	347.20	2.92	12.94	0.55
43	5/5/2018	S2A	-1.23	0.39	8.57	289.20	1.89	9.12	2.49
44	6/17/2018	OLI	-0.79	0.82	2.45	51.48	0.03	1.15	8.78
45	7/3/2018	OLI	-0.96	0.39	2.29	244.40	0.30	3.43	1.78
46	7/19/2018	OLI	-1.47	-0.19	2.64	69.16	0.02	1.57	3.05

1.4.2 Dominant drivers of SSC

Regressions between transect-averaged SSC and tidal parameters, wind speed, and river discharge were carried out in order to quantify the influence of each factor. Generally, SSC increased when the Parker River discharged more sediment into the bay (Fig. 1.12). River discharge explained only 19% of SSC variance, thereby indicating that other factors also controlled the distribution of SSC when the river discharge is low. Note also that only a few data points had high river discharge data ($> 3 \text{ m}^3/\text{s}$), which might have contributed to the lower R^2 of the regression.

Wind transfers energy to the water surface, generating waves whose shear stresses combined with tidal currents are responsible for sediment resuspension in shallow bays (Fagherazzi and Wiberg 2009). There was no clear relationship ($R^2 < 0.1$) between averaged SSC and wind speed (Fig. 1.13). However, removing three outliers with high SSC dominated either by extremely high river discharge (April 03, 2014) or very fast

water level variations dh/dt (April 03, 2014, May 10, 2016, June 17, 2018) would increase the R^2 to 0.40. In accordance with local wind climate (Fagherazzi et al. 2014), our study area was dominated by northeast and northwest winds (Fig. 1.14), but there was no obvious relationship between SSC and wind direction.

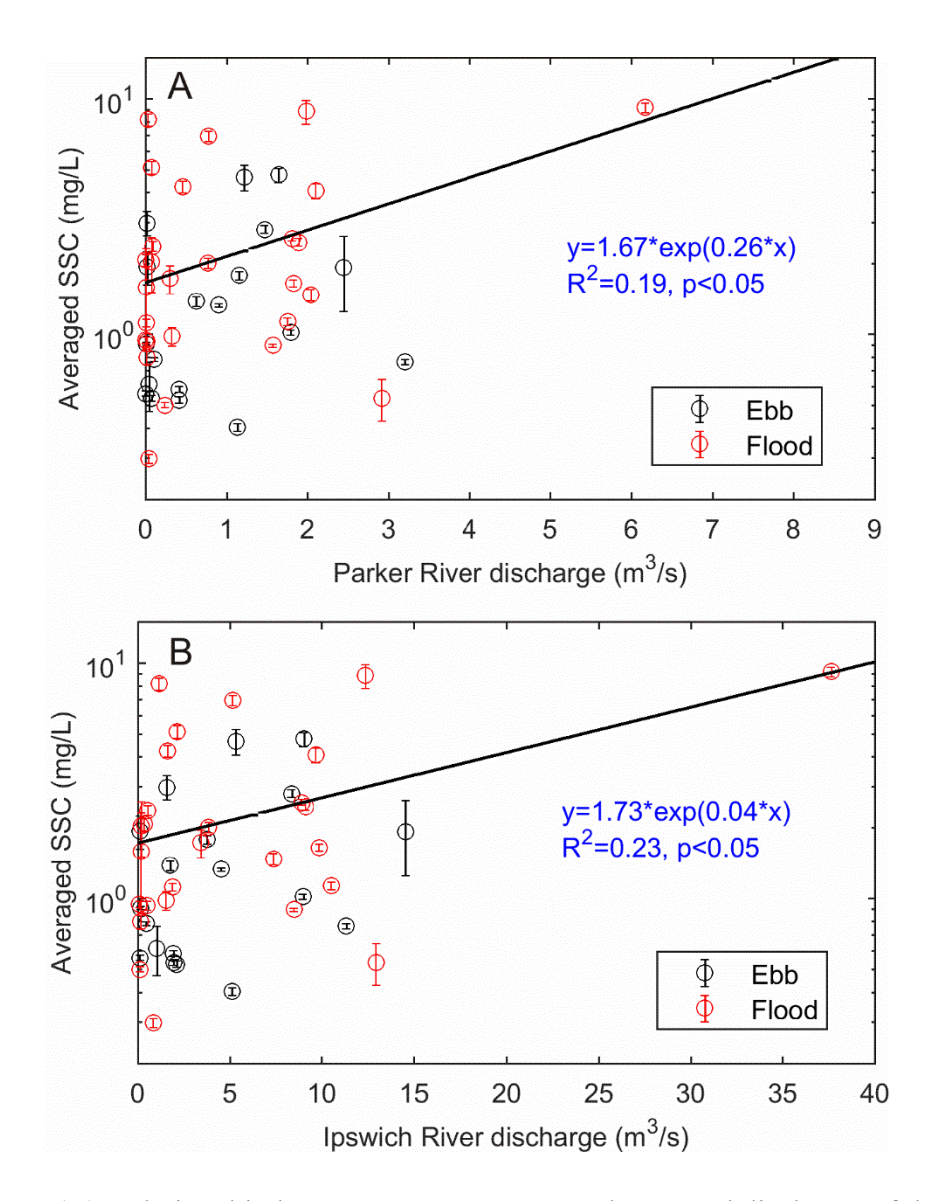


Figure 1.12 (A) Relationship between transect-averaged SSC and discharge of the Parker River; (B) between transect-averaged SSC and discharge of the Ipswich River.

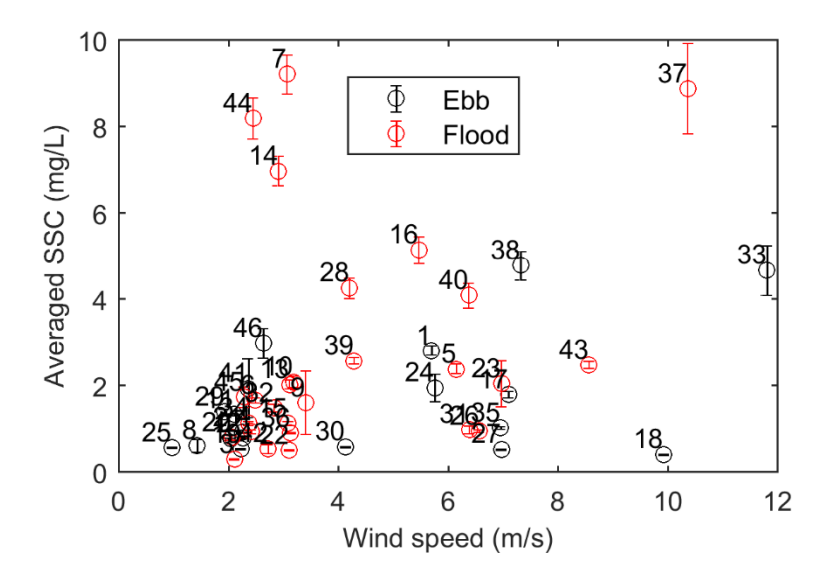


Figure 1.13 Relationship between transect-averaged SSC and wind speed; labeled number is the order of 46 scenes showed in Table 1.4.

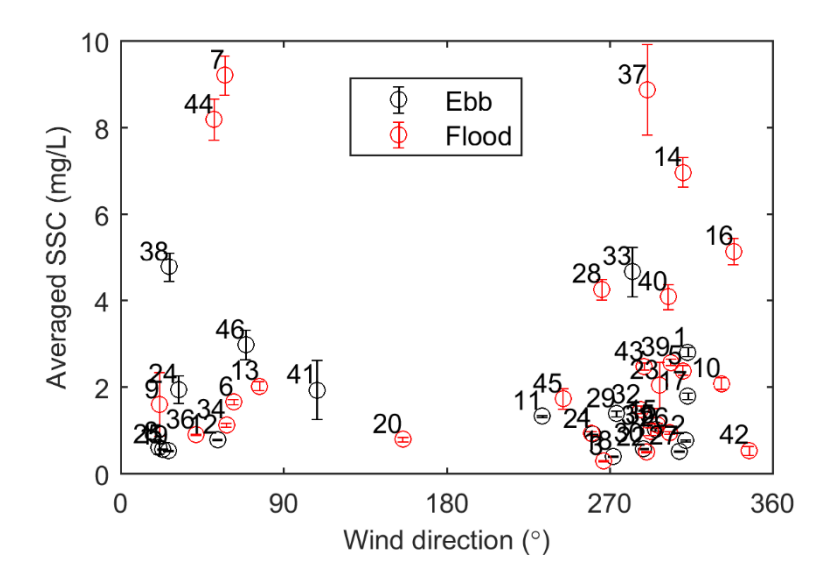


Figure 1.14 Relationship between transect-averaged SSC and wind direction; labeled number is the order of 46 scenes showed in Table 1.4.

A stronger correlation existed between transect-averaged SSC and water level variations dh/dt during tidal flood (Fig.1.15a), highlighting the control that tidal discharge played on SSC. Water level variations dh/dt explained approximately 19% of the overall variance of SSC. Furthermore, dh/dt explained 49% of the variance when only low water levels were considered (Fig. 1.15b). During ebb, the variation in water level dh/dt cannot explain variations in SSC at either low or high water levels (Fig. 1.15b,c). Generally, higher SSC occurred at low water levels (Fig. 1.16a). Water level h explained approximately 60% of the overall variance of SSC during ebb (Fig. 1.16b) and only 29% during flood (Fig. 1.16c).

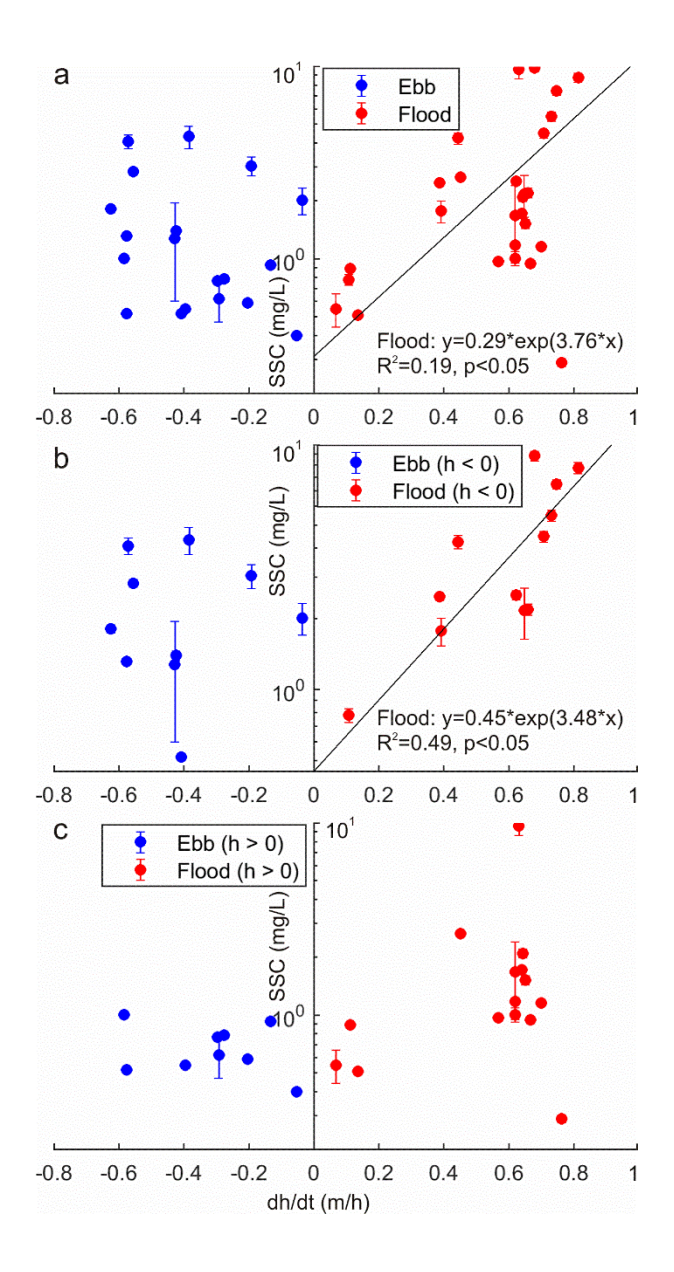


Figure 1.15 (a) Transect-averaged SSC as a function of variation in water level dh/dt in flood and ebb; (b) only during low water level (h < 0 m), and (c) only during high water level (h > 0 m).

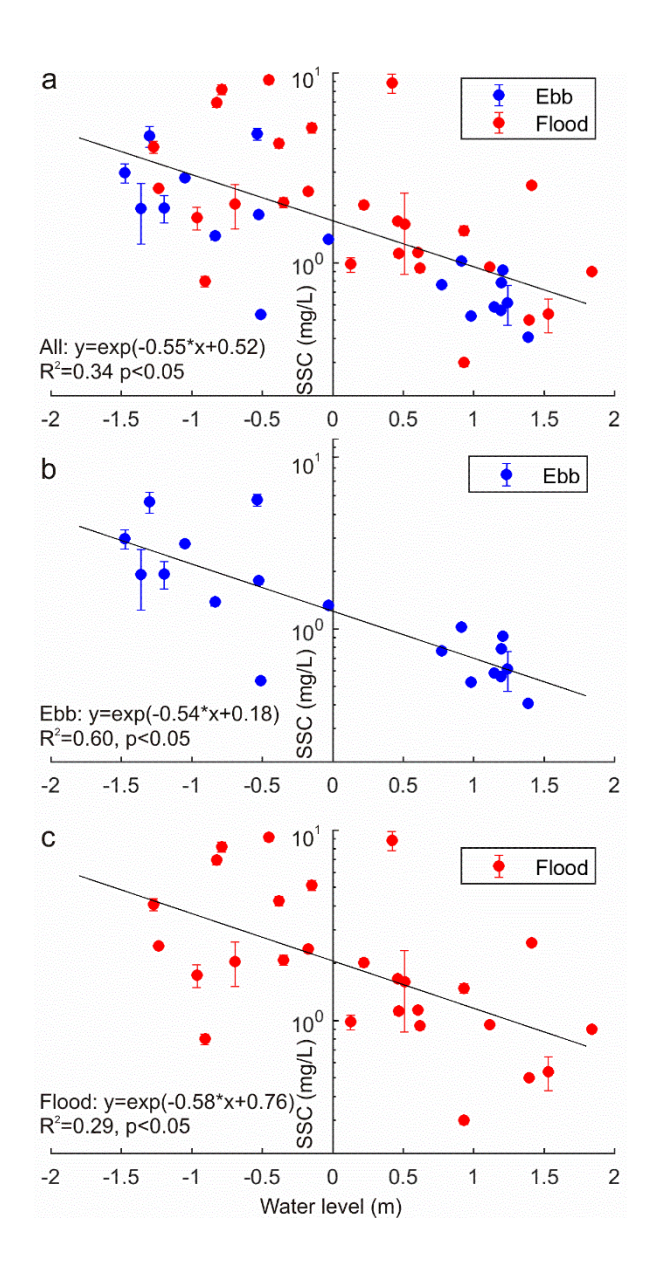


Figure 1.16 (a) Transect-averaged SSC as a function of water level h; (b) only during ebb tide (dh/dt < 0), and (c) only during flood tide (dh/dt > 0).

These results indicate that tidal flow (through its proxy dh/dt), wind speed, river discharge, and water level all contributed significantly to the observed dynamics of SSC along the entire transect. To spatially evaluate the contribution of each factor along the sound, we calculated the correlation coefficients between SSC and river discharge, dh/dt, wind

speed and water level along the transect (Fig. 1.17a). River discharge, variation of tidal water level dh/dt and water level dominated SSC, followed by wind speed. The river influence was stronger in the upper bay, while the variation in water level dh/dt, a proxy for tidal flow, had more influence in the middle of the sound. Finally, the effect of water level h increased moving offshore toward the inlet.

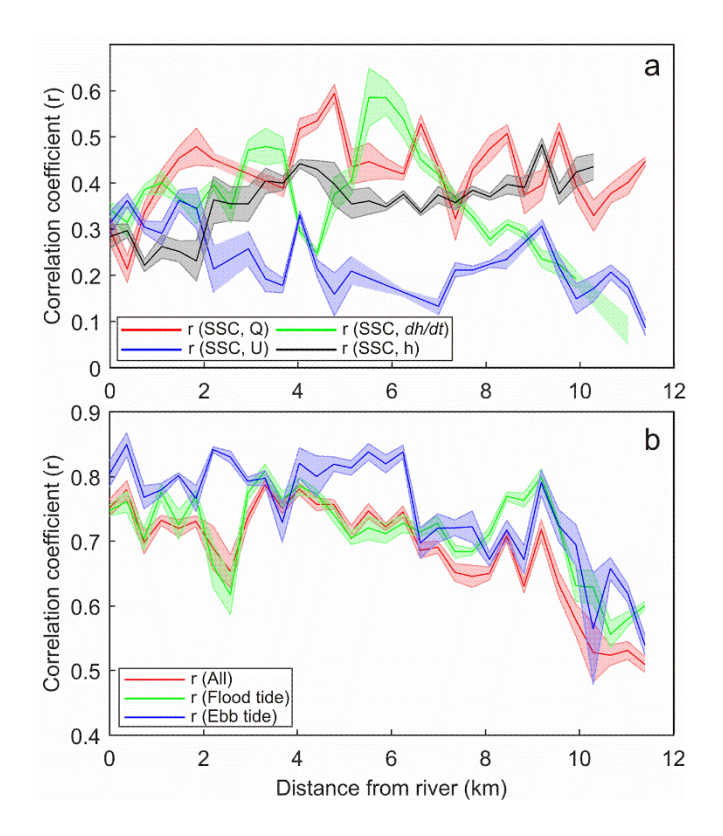


Figure 1.17 Correlation coefficients between SSC and river discharge (Q), variation of tidal water level (dh/dt), wind speed (U) and water level (h) along the main channel thalweg. (a) Correlation coefficients between SSC and SSC predicted using models of Eqs.1.14-1.16 at each location (also considering only flood and ebb) along the main channel thalweg. Shaded area around the lines indicate the 95% confidence interval.

1.4.3 Comparison of local algorithm developed in this study to SSA-L algorithm

Semi-analytical algorithms (SSA-L) for low concentrations ($Rrs \le 0.03 \text{ sr}^{-1}$) from Han et al. (2016) and Nechad et al. (2010) for Landsat8 OLI and Sentinel-2 MSI sensors.

$$SSC_{OLI} = 346.353 * \pi * Rrs_{OLI} (red) / (1 - \pi * Rrs_{OLI} (red) / 0.5)$$
(1.12)

$$SSC_{MSI} = 396.005 * \pi * Rrs_{MSI} (red) / (1 - \pi * Rrs_{MSI} (red) / 0.5)$$
(1.13)

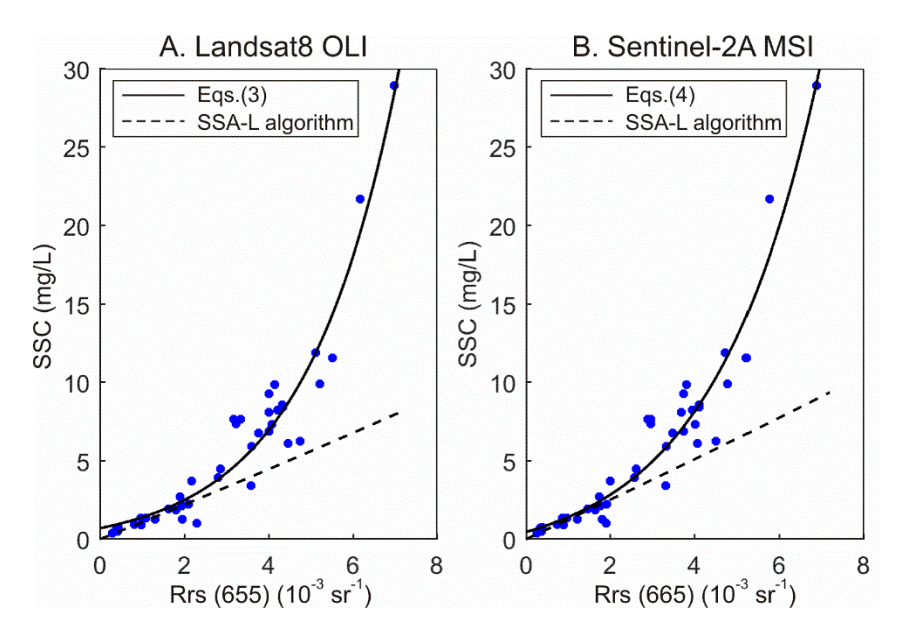


Figure 1.18 Comparison of our local empirical algorithms (Eqs. 1.3, 1.4) with the global semi-analytical algorithm SSA-L (Eqs. 1.12, 1.13) from Han et al. (2016) and Nechad et al. (2010) for both the Landsat-8 OLI (A) and the Sentinel-2A MSI (B).

1.4.4 Predicting SSC in the main channel thalweg

Since the combined effects of several factors control the distribution of SSC, we used three multivariate nonlinear regression models. One using all data:

$$ln(SSC) = 0.03Q + 0.58 \frac{dh}{dt} - 0.51h + 0.07U - 0.08$$

$$R^{2}=0.60, p\text{-value} << 0.001, n=46$$
(1.14)

One using only flood data:

$$ln(SSC) = 0.04Q + 1.50 \frac{dh}{dt} - 0.43h + 0.10U - 0.78$$
 (1.15)

$$R^{2}=0.56, p\text{-value} <<0.001, n=27$$

And one using only ebb data:

$$ln(SSC) = -0.57h + 0.22$$
 (1.16)
 $R^2 = 0.64, p\text{-value} << 0.001, n=19$

Where Q is total river discharge of Parker and Ipswich Rivers (m³/s), dh/dt is the water level variation (m/h), U is wind speed (m/s), and h is water level (m). Note all the variables in regression models are statistically significant (p-value <0.05).

Using all hydrodynamic and meteorological parameters, we computed the correlation coefficient between SSC and SSC predicted using models of Eqs. (1.14-1.16) at each location along the thalweg, as well as only during flood tide and only during ebb tide (Fig.

1.17b). Generally, the regression model showed a correlation coefficient larger than 0.7 in the middle and upper bay and a higher coefficient during ebb than during flood tide. The correlation coefficient became lower near the inlet (after 10 km), indicating that other processes were acting here, as for instance the supply of sediment from the ocean.

The regression model can be used to predict SSC along the bay for a given set of hydrodynamic and meteorological parameters. To evaluate the performance of the model, we show a validation of both transect averaged SSC for all images (Fig. 1.19a), and SSC at each location along the thalweg for three representative scenes covering the range of SSC values (Fig. 1.19b). Both analyses show more outliers at high values of SSC partly due to lack of training data for high SSC. These validation results demonstrate that high-resolution remote sensing imagery can be used to monitor and predict SSC in shallow coastal bays, facilitating the assessment of sediment budgets of these optically complex systems.

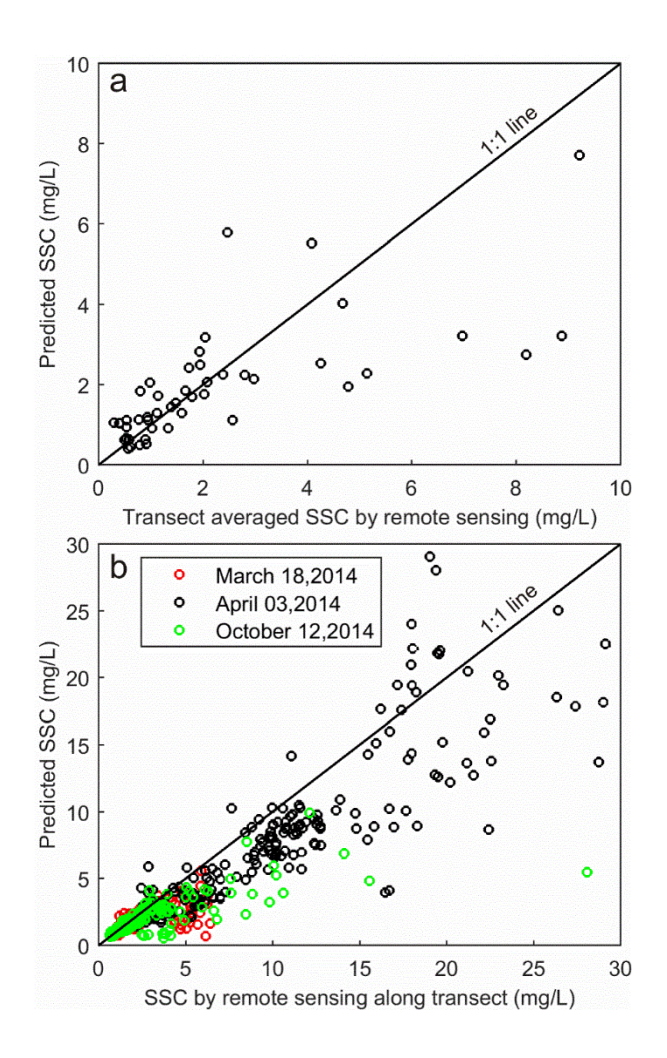


Figure 1.19 (a) Relationship between the remotely sensed SSC averaged along the main channel thalweg (n=46) and the corresponding values predicted from the model for all 46 remote-sensing scenes used in this study (Eq. 1.14), (b) discrete SSC along the main channel thalweg and corresponding predicted values from the models (Eqs. 1.14-1.16) for three representative scenes (n=187 for each scene).

1.5 Discussion

SSC maps derived from remote sensing images allow a quantitative assessment of sediment dynamics in shallow bay systems. For coastal bays with narrow channels (~ 1

km), only remote sensing imagery with high spatial resolution and a revisit time of hours could fully capture tidal and wave dynamics and the distribution of SSC in surface waters. Sentinel-2 and Landsat-8 haves a high resolution of 10 m and 30 m respectively, however the relatively long revisit time compared to tidal cycles has limited their application in studies of tidal flow and SSC dynamics. Therefore, most studies based on remote sensing of SSC in coastal areas focus on the retrieving method itself, with the goal of producing the most accurate SSC map. We compiled all the SSC maps from Landsat-8 and Sentinel-2 remote sensing imagery collected between 2013 and 2018, matched water level, tidal flow, and wind conditions to each image, and built the relationship between SSC and these physical drivers. Our study is one of few that quantitatively assesses the contributions of different hydrodynamic and meteorological drivers to SSC, and predicts spatial distribution of SSC under different conditions (see also Eleveld et al. 2014, Hudson et al., 2017).

Based on 631 samples with SSC ranging from 0.15 to 2600 mg/L collected in various coastal areas, Han et al. (2016) put forward a generic semi-analytical algorithm (SSA) for sediment concentration in global coastal waters and derived coefficients for different ocean color sensors including the Landsat-8 OLI and Sentinel-2 MSI (Nechad et al. 2010). Compared to our local empirical algorithms (Eqs.1.3, 1.4), their semi-analytical algorithms (Eqs.1.12, 1.13) underestimated SSC for large values (see Fig. 1.18). This discrepancy may due to the difference in the range of data used, as the maximum value of SSC in our study is only 28.94 mg/L. Moreover, the semi-analytical algorithm derived

with a large range of SSC may not capture well variations of SSC lower than 30 mg/L, as those occurring in the Plum Island Estuary.

Two possible processes explain the general decreasing trend in SSC seaward (Fig. 1.10, 1.11): riverine discharge and sediments resuspension in the upper bay. Fagherazzi et al. (2014) showed that the upper bay is characterized by tidal flats with fine grain sediments (mud and silt), that are more easily resuspended. Despite the freshwater discharge of the Parker River is relatively small compared to the tidal prism, the sediment load from the Parker river is significant, accounting for about 10% of total sediment sources in the system (Hopkinson et al. 2018). Flood dominance pushes sediments toward the upper part of the bay, trapping the sediment discharged from the Parker River. Estuarine turbidity maxima, common in estuaries, can also lead to an increase in SSC at the interplay zone of fresh and ocean waters (Dyer et al. 2004). In the Plum Island estuary, the turbidity maximum is located at the mouth of the Parker River (Hopkinson et al. 2018). Significant seasonal variations in SSC are present, with higher SSC occurring in spring due to river freshets triggered by snowmelt. In the Westerschelde estuary, Eleveld et al. (2014) found instead that the highest SSC occurs in winter due to stronger wind waves. In our mesotidal sound with limited fetch, the role of waves seems minor. The 46 images analyzed here capture a river flood in April 3, 2014 and a Nor'easter storm in March 26, 2018, shedding light on the role of extreme events (Fig. 1.9e, i).

The transect-averaged SSC is controlled by river discharge, tidal flow, wind, and water level. Water level and tidal flow (here represented by the variations in water level dh/dt)

are the two dominant factors controlling SSC at each point along the transect, followed by river discharge and wind speed. Our results are consistent with Hudson et al. (2017), who showed that waves only affect turbidity at the mouth of the Columbia River Estuary, but are less important than river discharge and tidal flow. River discharge dominates turbidity in the Columbia River Estuary, while in Plum Island Estuary tidal flow and water level are more important, since the rivers are small (see Fig. 1.12, 1.15,1.16). We also propose a multivariable regression model that predicts spatial SSC using simple hydrodynamic and meteorological parameters (Eq. 1.14-1.16 and Fig. 1.19). For tidally mixed shallow bay systems, such a model provides a potential way to evaluate sediment budgets and SSC dynamics even during extreme weather conditions.

A significant increase in SSC along the entire bay caused by a river flood is showed in Fig. 1.10c. This result highlights the role of infrequent hydrological events on sediment dynamics. High SSC triggered by the Nor'easter of March 26, 2018 (Fig. 1.10e) indicate that strong winds can also trigger sediment resuspension, but more along the shoreline rather than in the sound. Wave induced shear stresses could suspend bottom sediments, and enhance the exchange of sediments between tidal flats and channels. Castagno et al. (2018) modeled the influence of storms on sediment budgets at the Virginia Coast Reserve, USA, and found that intense storms resuspend and funnel fine-grained materials from the nearshore to the interior of the back-barrier tidal basins. In Plum Island Estuary, waves-induced sediment resuspension seems of secondary importance compared to tidal flows, water level, and sediment discharge from rivers.

Our results also show that the distribution of SSC is different between flood and ebb, with SSC higher during flood. As a result, the sound is importing and trapping sediments, which explains why the marsh accretion is keeping pace with SLR (Hopkinson et al. 2018). During ebb water levels become very important, exerting a very strong control on SSC (Fig. 1.16b). We ascribe this result to three possible factors: i) The peak velocity in salt marsh creeks is delayed during ebb, occurring at low water levels and mobilizing sediment on banks or stored at the bottom of the channels. In fact, water moves slowly on the vegetated marsh surface, so that the channels are still draining the marsh platform hours after high slack water (Fagherazzi et al. 2008). As a result, the stage-velocity relationship is very asymmetric (Bayliss-Smith et al. 1979). ii) Seepage from marsh banks during ebb can lead to local sediment piping and sapping, increasing the turbidity of the water exiting the marshes (Howes and Goehringer 1994). iii) Very shallow flows (up to 5cm depth) can mobilize soft sediments stored in mudflats along large tidal channels or at the bottom of small creeks dissecting the marsh (Fagherazzi and Mariotti 2012). During the late phase of salt marsh drainage, very shallow flows can be very fast, sometimes reaching supercritical conditions, because they are driven by bottom slope and not by tidal propagation. A similar phenomenon was observed in mudflats in Willapa Bay, Washington State, USA, where a turbid tidal edge carried sediment at very low water depths (Fagherazzi and Mariotti 2012). All the sediments mobilized by these three processes during marsh drainage will eventually reach the sound contributing to the turbidity of the water at low tide. However, the overall sediment flux is low, because the discharge is small when the water depth is limited. As a result, the sediment concentration during ebb does not spike, and remains lower than during flood (Fig. 1.11a). The influence of water depth increases downstream along the sound, probably because more turbid water from the marshes is collected (Fig. 1.17a).

SSC depends more on tidal current amplitudes and their variations in time during flood (Fig. 1.15). This result indicates that during flood tidal flow and related shear stresses mobilize bottom sediments, and carry them toward the upper bay. In the flood period from slack water to marsh inundation, variations of water level can explain 49% of SSC (e.g. Fagherazzi et al. 2013b). However, when the marsh is flooded, there is no relationship between water level variations and SSC (Fig. 1.15c). This highlights the complexity of tidal hydrodynamics and sediment transport pathways caused by the presence of salt marshes. This complexity prevents the establishment of a linear relationship between velocity and turbidity, as detected by remote sensing data in the lakes in the Peace-Athabasca Delta (Pavelsky and Smith, 2009).

Resuspension triggered by tidal flow seems peaking in the middle sound, where the correlation coefficient between dh/dt and SSC is maximum. The influence of dh/dt on sediment dynamics decreases near the inlet, where oceanic inputs of sediment are likely important (Fig. 1.17a). Note that herein we do not address sedimentary processes acting on the inner continental shelf, and therefore the predictive ability of our regression model decreases near the inlet (low r in Fig. 1.17).

Fagherazzi et al. (2013a) and Ganju et al. (2015) emphasized how a positive sediment budget is critical for the stability of salt marshes and coastal bays facing SLR (see also

Hopkinson et al. 2018). In fact, intertidal systems must trap sediment and accrete in order to counteract SLR. Ganju et al. (2015) suggested the use of flood/ebb SSC differential in marsh creeks to assess the vulnerability of salt marsh complexes. The same parameter can be scaled up to the entire Plum Island Estuary. Figure 1.11a shows that flood/ebb SSC differential is positive in the middle and upper section of the sound, indicating that the system is importing sediment and therefore partly mitigating the effect of SLR. Our methodology based on remote sensing images can therefore be used to quickly assess vulnerability of marshes and shallow bays to SLR. The data analyzed here span only 5 years and cannot capture in detail the interannual variability in SSC.

Herein we have used variations in water surface elevation as a coarse proxy for tidal flow, following the simple tub model of Boon (1975). However, tidal propagation and the presence of salt marshes give rise to tidal asymmetries that affect tidal discharge, velocity, and ultimately sediment advection and resuspension (Fagherazzi et al. 2008; Friedrichs and Aubrey 1988). Remote sensing images are not able to capture temporal dynamics of SSC such as sediment settling and advection. For example, sediment in suspension can take hours to settle, so that the sediment concentration measured at one instant might have originated from hydrodynamic conditions that occurred in the past. This is particularly true for waves and wind fields that can change in hours. Advection can also transport sediment away from the location where it was first resuspended. In this situation, simply attributing the increase in SSC in the channel to waves and strong tidal flows at the instant of the remote sensing image collection might introduce an error. This error likely affects the correlation between SSC and different drivers, especially wind waves. Water level is

also an important driver of SSC in the tidally dominated systems especially during ebb. Further research is deemed necessary to determine the importance of tidal asymmetry on the evaluation of sediment budgets from remote sensing images.

SSC of our 40 water samples ranges from 0 mg/L to 30 mg/L, covering the range of values measured in-situ in the last 13 years (Hopkinson et al. 2018). The empirical algorithm constructed captured a representative range of SSC concentrations for the entire bay, with the exception of very extreme events. During large river floods and energetic storms, SSC could fall outside the range covered in the study. This might cause uncertainty when our empirical relationship is used, although it would be very challenging to conduct *in situ* measurements during those conditions. It is also important to recognize that SSC retrieved from remote sensing can be affected by errors from the atmospheric correction (Warren et al., 2019).

1.6 Conclusions

In this paper, we demonstrated that the existing record of high-resolution imagery from Landsat-8 and Sentinel-2 can be used to quantitatively assess of the relative roles of hydrodynamical and meteorological drivers on the variability of suspended sediments in a marsh-influenced estuary. High-resolution images from these sensors provided snapshots of SSC distribution that are difficult to capture with *in situ* instruments in such dynamic and heterogenous systems. These data are crucial to decipher the relative role of different physical processes in driving suspended sediment dynamics. Here, the analysis

of high-resolution imagery revealed several important pieces of information about SSC dynamics in the Plum Island Estuary:

- (1) SSC generally decreases seaward in the sound, and is higher in the spring season because of increased river discharge caused by snowmelt.
- (2) Extreme events such as river floods and storms increased SSC by 5-to-10-fold, greatly altering the SSC distribution in the system. Wind direction was also found to be more important to sediment resuspension than wind speed.
- (3) Higher SSC occurs during tidal flood rather than ebb, especially during the spring and fall seasons. This tidal asymmetry possibly favors sediment retention in the bay, increasing the resilience of the marsh to sea level rise.
- (4) Water level, tidal flow and river discharge are generally the most important factors dominating SSC along the sound, followed by wind speed.

The Plum Island Estuary in Massachusetts was used herein as a prime example of a midlatitude, tidally-driven estuary influenced by large fluctuations in river discharge and regularly impacted by storms. However, this general approach is applicable to other estuaries around the world in order to determine the dominant drivers of SSC dynamics. This methodology can be useful to help quantify sediment budgets and assess the fate and sustainability of marshes. The Plum Island Estuary was particularly challenging because bottom reflectance prohibited the use of remote sensing over much of the estuary besides the main channel. Marsh-influenced systems with higher sediment loads (e.g., coastal Georgia and Louisiana, USA) would not be influenced as much by bottom reflectance and are therefore even more suitable for this analysis. Despite the long revisit-time of current high-resolution sensors onboard Landsat-8 and Sentinel-2, our study showed that the record of high-resolution imagery available since the beginning of Landsat-8 operations (May 2013) was sufficient to capture a representative range of tidal conditions, river floods and storms. This is true even considering that Sentinel-2A and -2B MSI (in operation since 2015 and 2017, respectively) contributed to only part of the 5-year record used in this study. With these three satellite sensors now operating, new sensors launching soon (e.g., Landsat-9), and constantly improving atmospheric correction procedures (Warren et al., 2019), the record of usable high-resolution imagery is bound to be rapidly expanding and to provide an even more representative depiction of suspended dynamics in these important coastal systems.

1.7 References

Antoine, D., Hooker, S.B., Bélanger, S., Matsuoka, A., Babin, M., 2013. Apparent optical properties of the Canadian Beaufort Sea – Part 1: Observational overview and water column relationships. Biogeosciences 10, 4493–4509. DOI: 10.5194/bg-10-4493-2013

Bailey, S. W., Franz, B. A., & Werdell, P. J. (2010). Estimation of near-infrared water-leaving reflectance for satellite ocean color data processing. Optics express, 18(7), 7521-7527. DOI: 10.1364/OE.18.007521

Bayliss-Smith, T.P., Healey, R., Lailey, R., Spencer, T. and Stoddart, D.R., 1979. Tidal flows in salt marsh creeks. Estuarine and Coastal Marine Science, 9(3), pp.235-255. DOI: 10.1016/0302-3524(79)90038-0

Blum, M.D., & Roberts, H.H. (2009). Drowning of the Mississippi Delta due to insufficient sediment supply and global sea-level rise. Nature Geoscience, 2, 488-491. DOI:10.1038/NGEO553

Boon III, J.D., 1975. Tidal discharge asymmetry in a salt marsh drainage system 1, 2. Limnology and Oceanography, 20(1), pp.71-80. DOI: 10.4319/lo.1975.20.1.0071

- Cao, Z., Duan, H., Feng, L., Ma, R., & Xue, K. (2017). Climate-and human-induced changes in suspended particulate matter over Lake Hongze on short and long timescales. Remote sensing of environment, 192, 98-113. DOI: 10.1016/j.rse.2017.02.007
- Carr, J.A., D'Odorico, P., McGlathery, K.J., & Wiberg, P.L. (2016). Spatially explicit feedbacks between seagrass meadow structure, sediment and light: Habitat suitability for seagrass growth. Advances in Water Resources, 93, 315-325. DOI: 10.1016/j.advwatres.2015.09.001
- Castagno, K. A., Jiménez-Robles, A. M., Donnelly, J. P., Wiberg, P. L., Fenster, M. S., & Fagherazzi, S. (2018). Intense storms increase the stability of tidal bays. Geophysical Research Letters, 45(11), 5491-5500. DOI: 10.1029/2018GL078208
- Claessens, L., Hopkinson, C., Rastetter, E., & Vallino, J. (2006). Effect of historical changes in land use and climate on the water budget of an urbanizing watershed. Water Resources Research, 42(3). DOI: 10.1029/2005WR004131
- Constantin, S., Doxaran, D., Derkacheva, A., Novoa, S., & Lavigne, H. (2018). Multitemporal dynamics of suspended particulate matter in a macro-tidal river Plume (the Gironde) as observed by satellite data. Estuarine, Coastal and Shelf Science, 202, 172-184. DOI: 10.1016/j.ecss.2018.01.004
- De Swart, H. E., Schuttelaars, H. M., & Talke, S. A. (2009). Initial growth of phytoplankton in turbid estuaries: A simple model. Continental Shelf Research, 29(1), 136-147. DOI: 10.1016/j.csr.2007.09.006
- D'Sa, E. J., Miller, R. L., & McKee, B. A. (2007). Suspended particulate matter dynamics in coastal waters from ocean color: Application to the northern Gulf of Mexico. Geophysical Research Letters, 34(23). DOI: 10.1029/2007GL031192
- Dai, Z., Fagherazzi, S., Mei, X., & Gao, J. (2016). Decline in suspended sediment concentration delivered by the Changjiang (Yangtze) River into the East China Sea between 1956 and 2013. Geomorphology, 268, 123-132. DOI: 10.1016/j.geomorph.2016.06.009
- Dyer, K. R., Christie, M. C., & Manning, A. J. (2004). The effects of suspended sediment on turbulence within an estuarine turbidity maximum. Estuarine, Coastal and Shelf Science, 59(2), 237-248. DOI: 10.1016/j.ecss.2003.09.002
- Eleveld, M.A., van der Wal, D., & van Kessel, T. (2014). Estuarine suspended particulate matter concentrations from sun-synchronous satellite remote sensing: Tidal and meteorological effects and biases. Remote sensing of environment, 143, 204-215. DOI: 10.1016/j.rse.2013.12.019
- Everett, J. D., Baird, M. E., Oke, P. R., & Suthers, I. M. (2012). An avenue of eddies: Quantifying the biophysical properties of mesoscale eddies in the Tasman Sea. Geophysical Research Letters, 39(16). DOI: 10.1029/2012GL053091

Fagherazzi, S., Hannion, M. and D'Odorico, P., 2008. Geomorphic structure of tidal hydrodynamics in salt marsh creeks. Water resources research, 44(2). DOI: 10.1029/2007WR006289

Fagherazzi, S. and Mariotti, G., 2012. Mudflat runnels: Evidence and importance of very shallow flows in intertidal morphodynamics. Geophysical Research Letters, 39(14). DOI: 10.1029/2012GL052542

Fagherazzi, Edmonds, D.A., Nardin, W., Leonardi, N., Canestrelli, A., Falcini, F., Jerolmack, D.J., Mariotti, G., Rowland, J.C., & Slingerland, R.L. (2015). Dynamics of river mouth deposits. Reviews of Geophysics, 53, 642-672. DOI: 10.1002/2014RG000451

Fagherazzi, Kirwan, M.L., Mudd, S.M., Guntenspergen, G.R., Temmerman, S., D'Alpaos, A., van de Koppel, J., Rybczyk, J.M., Reyes, E., Craft, C., & Clough, J. (2012). Numerical models of salt marsh evolution: Ecological, geomorphic, and climatic factors. Reviews of Geophysics, 50. DOI: 10.1029/2011RG000359

Fagherazzi, Mariotti, G., Banks, A.T., Morgan, E.J., & Fulweiler, R.W. (2014). The relationships among hydrodynamics, sediment distribution, and chlorophyll in a mesotidal estuary. Estuarine, Coastal and Shelf Science, 144, 54-64. DOI: 10.1016/j.ecss.2014.04.003

Fagherazzi, S., Mariotti, G., Wiberg, P.L. and McGlathery, K.J., (2013a). Marsh collapse does not require sea level rise. Oceanography, 26(3), pp.70-77. DOI: 10.5670/oceanog.2013.47

Fagherazzi, S. and Priestas, A.M., 2010. Sediments and water fluxes in a muddy coastline: interplay between waves and tidal channel hydrodynamics. Earth Surface Processes and Landforms, 35(3), pp.284-293. DOI: Fagherazzi, S., Wiberg, P. L., Temmerman, S., Struyf, E., Zhao, Y., & Raymond, P. A. (2013b). Fluxes of water, sediments, and biogeochemical compounds in salt marshes. Ecological Processes, 2(1). DOI: 10.1002/esp.1909

Fagherazzi, S., Viggato, T., Vieillard, A.M., Mariotti, G. and Fulweiler, R.W., 2017. The effect of evaporation on the erodibility of mudflats in a mesotidal estuary. Estuarine, Coastal and Shelf Science, 194, pp.118-127. DOI: 10.1016/j.ecss.2017.06.011

Fettweis, M.P., & Nechad, B. (2010). Evaluation of in situ and remote sensing sampling methods for SPM concentrations, Belgian continental shelf (southern North Sea). Ocean Dynamics, 61, 157-17. DOI: 10.1007/s10236-010-0310-6

Fichot, C.G., Downing, B.D., Bergamaschi, B.A., Windham-Myers, L., Marvin-DiPasquale, M., Thompson, D.R., & Gierach, M.M. (2016). High-Resolution Remote Sensing of Water Quality in the San Francisco Bay-Delta Estuary. Environ Sci Technol, 50, 573-583. DOI: 10.1021/acs.est.5b03518

- Friedrichs, C.T., & Aubrey, D.G. (1988). Non-linear tidal distortion in shallow well-mixed estuaries: a synthesis. Estuarine, Coastal and Shelf Science, 27, 521-545. DOI: 10.1016/0272-7714(88)90082-0
- Ganju, Defne, Z., Kirwan, M.L., Fagherazzi, S., D'Alpaos, A., & Carniello, L. (2017). Spatially integrative metrics reveal hidden vulnerability of microtidal salt marshes. Nature communications, 8, ncomms14156. DOI: 10.1038/ncomms14156
- Ganju, N.K., Kirwan, M.L., Dickhudt, P.J., Guntenspergen, G.R., Cahoon, D.R., & Kroeger, K.D. (2015). Sediment transport-based metrics of wetland stability. Geophysical Research Letters, 42, 7992-8000. DOI: 10.1002/2015GL065980
- Gernez, P., Lafon, V., Lerouxel, A., Curti, C., Lubac, B., Cerisier, S., & Barillé, L. (2015). Toward Sentinel-2 High Resolution Remote Sensing of Suspended Particulate Matter in Very Turbid Waters: SPOT4 (Take5) Experiment in the Loire and Gironde Estuaries. Remote Sensing, 7, 9507-9528. DOI: 10.3390/rs70809507
- Giardino, C., Oggioni, A., Bresciani, M., & Yan, H. (2010). Remote sensing of suspended particulate matter in Himalayan lakes. Mountain Research and Development, 30(2), 157-169. DOI: 10.1659/MRD-JOURNAL-D-09-00042.1
- Han, B., Loisel, H., Vantrepotte, V., Mériaux, X., Bryère, P., Ouillon, S., & Zhu, J. (2016). Development of a semi-analytical algorithm for the retrieval of suspended particulate matter from remote sensing over clear to very turbid waters. Remote Sensing, 8(3), 211. DOI: 10.3390/rs8030211
- Hein, C.J., FitzGerald, D.M., Carruthers, E.A., Stone, B.D., Barnhardt, W.A., & Gontz, A.M. (2012). Refining the model of barrier island formation along a paraglacial coast in the Gulf of Maine. Marine Geology, 307-310, 40-57. DOI: 10.1016/j.margeo.2012.03.001
- Hooker, S.B., Morrow, J.H., Matsuoka, A., 2013. Apparent optical properties of the Canadian Beaufort Sea Part 2: The 1% and 1 cm perspective in deriving and validating AOP data products. Biogeosciences 10, 4511–4527. DOI: 10.5194/bg-10-4511-2013
- Hopkinson, C.S., Morris, J.T., Fagherazzi, S., Wollheim, W.M., & Raymond, P.A. (2018). Lateral Marsh Edge Erosion as a Source of Sediments for Vertical Marsh Accretion. Journal of Geophysical Research: Biogeosciences, 123, 2444-2465. DOI: 10.1029/2017JG004358
- Howes, B.L. and Goehringer, D.D., 1994. Porewater drainage and dissolved organic carbon and nutrient losses through the intertidal creek banks of a New England salt marsh. Marine ecology progress series. Oldendorf, 114(3), pp.289-301.
- Hudson, A. S., Talke, S. A., & Jay, D. A. (2017). Using satellite observations to characterize the response of estuarine turbidity maxima to external forcing. Estuaries and coasts, 40(2), 343-358. DOI: 10.1007/s12237-016-0164-3

- Jay, D. A., Talke, S. A., Hudson, A., & Twardowski, M. (2015). Estuarine turbidity maxima revisited: Instrumental approaches, remote sensing, modeling studies, and new directions. In Developments in sedimentology (Vol. 68, pp. 49-109). Elsevier. DOI: 10.1016/B978-0-444-63529-7.00004-3
- Kearney, W.S., Mariotti, G., Deegan, L.A. and Fagherazzi, S., 2017. Stage-discharge relationship in tidal channels. Limnology and Oceanography: Methods, 15(4), pp.394-407. DOI: 10.1002/lom3.10168
- Kirwan, M. L., & Murray, A. B. (2007). A coupled geomorphic and ecological model of tidal marsh evolution. Proceedings of the National Academy of Sciences, 104(15), 6118-6122. DOI: 10.1073/pnas.0700958104
- Kirwan, M. L., Temmerman, S., Skeehan, E. E., Guntenspergen, G. R., & Fagherazzi, S. (2016). Overestimation of marsh vulnerability to sea level rise. Nature Climate Change, 6(3), 253-260. DOI: 10.1038/NCLIMATE2909
- Lawson, S. E., Wiberg, P. L., McGlathery, K. J., & Fugate, D. C. (2007). Wind-driven sediment suspension controls light availability in a shallow coastal lagoon. Estuaries and Coasts, 30(1), 102-112. DOI: 10.1007/BF02782971
- Li, J., & Zhang, C. (1998). Sediment resuspension and implications for turbidity maximum in the Changjiang Estuary. Marine Geology, 148, 117-124. DOI: 10.1016/S0025-3227(98)00003-6
- Mao, Z., Chen, J., Pan, D., Tao, B., & Zhu, Q. (2012). A regional remote sensing algorithm for total suspended matter in the East China Sea. Remote sensing of environment, 124, 819-831. DOI: 10.1016/j.rse.2012.06.014
- Mariotti, G., Fagherazzi, S., Wiberg, P. L., McGlathery, K. J., Carniello, L., & Defina, A. (2010). Influence of storm surges and sea level on shallow tidal basin erosive processes. Journal of Geophysical Research: Oceans, 115(C11). DOI: 10.1029/2009JC005892
- Miller, R.L., & McKee, B.A. (2004). Using MODIS Terra 250 m imagery to map concentrations of total suspended matter in coastal waters. Remote sensing of environment, 93, 259-266. DOI: 10.1016/j.rse.2004.07.012
- Mobley, C. D. (1999). Estimation of the remote-sensing reflectance from above-surface measurements. Applied optics, 38(36), 7442-7455. DOI: 10.1364/AO.38.007442
- Morrow, J. H., Booth, C. R., Lind, R. N., & Hooker, S. B. (2010). The compact-optical profiling system (C-OPS). Advances in Measuring the Apparent Optical Properties (AOPs) of Optically Complex Waters, NASA Tech. Memo, 215856, 42-50.
- Nechad, B., Ruddick, K.G., Park, Y., 2010. Remote Sensing of Environment Calibration and validation of a generic multisensor algorithm for mapping of total

- suspended matter in turbid waters. Remote Sens. Environ. 114, 854–866. DOI: 10.1016/j.rse.2009.11.022
- Neukermans, G., Ruddick, K., Loisel, H., Roose, P., 2012. Optimization and quality control of suspended particulate matter concentration measurement using turbidity measurements. Limnol. Oceanogr. Methods 10, 1011–1023. DOI: 10.4319/lom.2012.10.1011
- Pahlevan, N., Smith, B., Binding, C., & O'Donnell, D. M. (2017a). Spectral band adjustments for remote sensing reflectance spectra in coastal/inland waters. Optics Express, 25(23), 28650-28667. DOI: 10.1364/OE.25.028650
- Pahlevan, N., Sarkar, S., Franz, B. A., Balasubramanian, S. V., & He, J. (2017b). Sentinel-2 MultiSpectral Instrument (MSI) data processing for aquatic science applications: Demonstrations and validations. Remote sensing of environment, 201, 47-56. DOI: 10.1016/j.rse.2017.08.033
- Pavelsky, T. M., & Smith, L. C. (2009). Remote sensing of suspended sediment concentration, flow velocity, and lake recharge in the Peace Athabasca Delta, Canada. Water Resources Research, 45(11). DOI: 10.1029/2008WR007424
- Ribbe, J., Toaspern, L., Wolff, J. O., & Ismail, M. F. A. (2018). Frontal eddies along a western boundary current. Continental Shelf Research, 165, 51-59. DOI: 10.1016/j.csr.2018.06.007
- Staneva, J., Stanev, E.V., Wolff, J.-O., Badewien, T.H., Reuter, R., Flemming, B., Bartholomä, A., & Bolding, K. (2009). Hydrodynamics and sediment dynamics in the German Bight. A focus on observations and numerical modelling in the East Frisian Wadden Sea. Continental Shelf Research, 29, 302-319. DOI: 10.1016/j.csr.2008.01.006
- Snyder, J., Boss, E., Weatherbee, R., Thomas, A. C., Brady, D., & Newell, C. (2017). Oyster aquaculture site selection using Landsat 8-Derived Sea surface temperature, turbidity, and chlorophyll a. Frontiers in Marine Science, 4, 190. DOI: 10.3389/fmars.2017.00190
- Syvitski, J.P.M., Kettner, A.J., Overeem, I., Hutton, E.W.H., Hannon, M.T., Brakenridge, G.R., Day, J., Vörösmarty, C., Saito, Y., Giosan, L., & Nicholls, R.J. (2009). Sinking deltas due to human activities. Nature Geoscience, 2, 681-686. DOI: 10.1038/ngeo629
- Traykovski, P., Geyer, W. R., Irish, J. D., & Lynch, J. F. (2000). The role of wave-induced density-driven fluid mud flows for cross-shelf transport on the Eel River continental shelf. Continental Shelf Research, 20(16), 2113-2140. DOI: 10.1016/S0278-4343(00)00071-6

van der Wegen, M. (2013). Numerical modeling of the impact of sea level rise on tidal basin morphodynamics. Journal of Geophysical Research: Earth Surface, 118(2), 447-460. DOI: 10.1002/jgrf.20034

Vanhellemont, Q., & Ruddick, K. (2014). Turbid wakes associated with offshore wind turbines observed with Landsat 8. Remote Sensing of Environment, 145, 105-115. DOI: 10.1016/j.rse.2014.01.009

Walling, D.E. (2006). Human impact on land—ocean sediment transfer by the world's rivers. Geomorphology, 79, 192-216. DOI: 10.1016/j.geomorph.2006.06.019

Warren M. A., et al. (2019). Assessment of atmospheric correction algorithms for the Sentinel-2A MultiSpectral Imager over coastal and inland waters. Remote Sensing of Environment, 225, 267-289. DOI: 10.1016/j.rse.2019.03.018

Wiberg, P. L., Fagherazzi, S., & Kirwan, M. L. (2020). Improving predictions of salt marsh evolution through better integration of data and models. Annual review of marine science, 12, 389-413. DOI: 10.1146/annurev-marine-010419-010610

Widdows, J., Brinsley, M. D., Bowley, N., & Barrett, C. (1998). A benthic annular flume forin situmeasurement of suspension feeding/biodeposition rates and erosion potential of intertidal cohesive sediments. Estuarine, Coastal and Shelf Science, 46(1), 27-38. DOI: 10.1006/ecss.1997.0259

Winterwerp, J. C. (2002). On the flocculation and settling velocity of estuarine mud. Continental shelf research, 22(9), 1339-1360. DOI: 10.1016/S0278-4343(02)00010-9

Yang, S.L., Milliman, J.D., Li, P., & Xu, K. (2011). 50,000 dams later: Erosion of the Yangtze River and its delta. Global and Planetary Change, 75, 14-20. DOI: 10.1016/j.gloplacha.2010.09.006

Zhao, L., Chen, C., Vallino, J., Hopkinson, C., Beardsley, R.C., Lin, H., & Lerczak, J. (2010). Wetland-estuarine-shelf interactions in the Plum Island Sound and Merrimack River in the Massachusetts coast. Journal of Geophysical Research, 115. DOI: 10.1029/2009JC006085

Zhang, X., Leonardi, N., Donatelli, C. and Fagherazzi, S., 2019. Fate of cohesive sediments in a marsh-dominated estuary. Advances in Water Resources, 125, pp.32-40. DOI: 10.1016/j.advwatres.2019.01.003